

Review

Open Access



# Pressure-assisted crystallization techniques for high-performance metal halide perovskite devices

Yuan Yu<sup>1</sup>, Huitian Du<sup>2</sup>, Qiang Liu<sup>3</sup>, Zhiyong Pang<sup>4</sup>

<sup>1</sup>School of Physics, Shandong University, Jinan 250100, Shandong, China.

<sup>2</sup>School of Information and Electronic Engineering, Shandong Technology and Business University, Yantai 264005, Shandong, China.

<sup>3</sup>Shandong Yunhai Guochuang Innovative Technology Co., Ltd, Jinan 250000, Shandong, China.

<sup>4</sup>School of Integrated Circuits, Shandong University, Jinan 250100, Shandong, China.

**Correspondence to:** Prof. Zhiyong Pang, School of Integrated Circuits, Shandong University, 27 Shanda South Road, Licheng District, Jinan 250100, Shandong, China. E-mail: pang@sdu.edu.cn

**How to cite this article:** Yu, Y.; Du, H.; Liu, Q.; Pang, Z. Pressure-assisted crystallization techniques for high-performance metal halide perovskite devices. *Microstructures* 2025, 5, 2025046. <https://dx.doi.org/10.20517/microstructures.2024.144>

**Received:** 2 Dec 2024 **First Decision:** 6 Feb 2025 **Revised:** 13 Feb 2025 **Accepted:** 27 Feb 2025 **Published:** 17 Apr 2025

**Academic Editor:** Zhihua Sun **Copy Editor:** Fangling Lan **Production Editor:** Fangling Lan

## Abstract

The Pressure-assisted crystallization (PAC) technique has evolved alongside the development of metal halide perovskite materials, effectively harnessing the soft lattice characteristics of perovskites and integrating with thermal processing methods to enable the transformation of perovskite materials from fine grains into quasi-single crystals. This technique has led to significant improvements in the performance of perovskite functional devices. In recent years, a wealth of research on the PAC technique has emerged, and this paper provides a comprehensive review of these studies. The review systematically explores the role of the PAC process in perovskite materials from three key aspects: the mechanism of PAC, the effect of PAC, and the application of PAC in devices. It highlights how pressure significantly enhances the quality of perovskite films and wafers, as well as the performance of related devices, by promoting grain growth, merging grain boundaries, and eliminating voids. Finally, the paper assesses the challenges faced by PAC techniques and offers a forward-looking perspective on their future development.

**Keywords:** Pressure-assisted, crystallization, thermal treatment, metal halide perovskite, functional devices



© The Author(s) 2025. **Open Access** This article is licensed under a Creative Commons Attribution 4.0 International License (<https://creativecommons.org/licenses/by/4.0/>), which permits unrestricted use, sharing, adaptation, distribution and reproduction in any medium or format, for any purpose, even commercially, as long as you give appropriate credit to the original author(s) and the source, provide a link to the Creative Commons license, and indicate if changes were made.



## INTRODUCTION

Since the introduction of organic-inorganic hybrid perovskite materials in dye-sensitized solar cells in 2009<sup>[1]</sup>, perovskite solar cell has rapidly emerged as a significant milestone in the field of photovoltaics. Benefiting from the unique optoelectronic properties of perovskite materials<sup>[2]</sup> and their diverse solution-processable fabrication techniques<sup>[3-5]</sup>, photovoltaic devices based on these materials have progressively approached the efficiency levels of commercial silicon-based solar cells<sup>[6]</sup>, while demonstrating significant advantages in manufacturing costs<sup>[7]</sup> and flexibility. As a result, Perovskite solar cell has been widely recognized by both academia and industry as one of the core directions for next-generation photovoltaic development. The rapid advancement of perovskite solar cells has also catalyzed the extensive application of perovskite materials in other functional devices. Currently, perovskite materials have shown tremendous application potential in various fields, including photodetectors<sup>[8,9]</sup>, light-emitting diodes (LEDs)<sup>[10]</sup>, X-ray detectors<sup>[11]</sup>, artificial synapses<sup>[12]</sup>, and spin valves<sup>[13]</sup>. Notably, the annual publication volume of perovskite-related research continues to rank among the top in materials science, a trend that not only reflects the scientific value of this material system but also drives the in-depth development of functional devices based on perovskite materials.

The multifunctionality of perovskite materials is closely related to their tunable chemical composition and structure<sup>[14]</sup>. In recent years, many studies on material composition engineering have significantly enhanced the functional properties<sup>[15-17]</sup>. Moreover, pressure engineering, as an important thermodynamic method for studying perovskite materials, has received increasing attention. Under high-pressure conditions, bond lengths and bond angles in perovskite crystals change, leading to phase transitions and alterations in physical properties such as bandgap and exciton binding energy<sup>[18-20]</sup>. This is crucial for understanding the relationship between material structure and its physical properties. Furthermore, high pressure can induce unique physical phenomena<sup>[21-24]</sup>, providing valuable insights for designing and predicting novel functional materials. However, in practice, the new physical phenomena induced by high pressure do not persist once the pressure is released<sup>[25,26]</sup>. Although some studies have shown that, upon the release of high pressure, perovskite crystals transition from an amorphous state back to their normal room-temperature structure, resulting in some improvement in crystallinity and stability<sup>[27,28]</sup>, these enhancements are relatively limited. Furthermore, high-pressure techniques are not economically viable and are challenging to implement in practical applications. In contrast, at relatively lower pressures ( $101 \text{ kPa} < P < 1 \text{ GPa}$ ), especially when combined with thermal assistance, pressure has little effect on the material's structure but can significantly improve the crystallinity of perovskite polycrystalline materials, even showing quasi-single-crystal characteristics. Under certain conditions, it is capable of directing its crystal morphology to attain a desired morphology.

The crystallinity of perovskite materials is closely linked to their optoelectronic performance, thermoelectric properties, and stability properties<sup>[29-31]</sup>. Preparing low-cost, high-crystallinity perovskite polycrystalline is essential for various functional devices based on perovskite materials. In recent years, numerous studies have focused on improving material crystallinity, including controlling the crystallization process using high-boiling-point solvents<sup>[32,33]</sup> and anti-solvents<sup>[34-36]</sup>, introducing additives (crosslinkers<sup>[37,38]</sup>, Lewis bases<sup>[39,40]</sup>), designing post-film treatment methods such as different types of annealing treatments<sup>[41-43]</sup>, employing gas-assisted crystallization techniques like air knives<sup>[44-49]</sup>, and utilizing advanced vapor deposition equipment<sup>[50]</sup>. However, due to the lack of strong thermodynamic intervention, the crystallinity improvements brought about by solvent engineering, additive engineering, and conventional post-annealing processes are limited. Additionally, vapor deposition equipment is suitable only for preparing heat-resistant materials and is expensive. The pressure-assisted crystallization (PAC) technique can overcome these limitations and has broad applicability. It works universally for both 2D<sup>[51]</sup> and 3D

perovskite materials<sup>[52]</sup>, and previous studies show its application not only with rigid substrates but also with flexible substrate devices. Moreover, it has also demonstrated potential for large-area processing<sup>[53]</sup>. Research on the PAC process of perovskite materials plays a crucial role in developing high-performance functional devices.

Previous reviews have addressed the effects of pressure on perovskite crystals, primarily focusing on structural changes under high pressure (> 1 GPa) and the exploration of novel physical mechanisms<sup>[54-56]</sup>. This paper focuses on the enhancement of crystallinity in perovskite materials through PAC, reviewing recent advancements from three key perspectives: pressure-assisted processing equipment and crystallization mechanisms, the effects of PAC, and its applications in devices. The aim is to systematically elucidate the role of pressure-assisted crystallization in perovskite materials, highlighting how pressure can significantly improve the quality of perovskite films by promoting grain growth, reducing defect density, and eliminating voids, thereby enhancing the performance of related devices. Additionally, we discuss the challenges facing the development of the PAC technique and offer reasonable expectations for its future progress.

## PRESSURE-ASSISTED CRYSTALLIZATION EQUIPMENT AND MECHANISM

### Pressure-assisted crystallization equipment

In recent years, a large number of studies on PAC of perovskite have emerged. Due to the lack of standardized equipment, the equipment reported in the literature varies significantly. It is therefore necessary to introduce pressure-assisted processing equipment. We categorize these pressure devices into two types. The first type is the open system, characterized by the application of mechanical pressure to the original film or microcrystals through a platen, with the pressing chamber being open to the atmosphere. This equipment is similar to the table press. A typical pressing device, as shown in [Figure 1A](#), applies uniaxial pressure<sup>[52]</sup>. The second type is the closed system, where the platen does not directly apply pressure to perovskite films. Instead, the films are placed inside a sealed chamber filled with a pressure-transmitting liquid (such as high-viscosity silicone oil<sup>[51]</sup>), with a movable chamber lid on top. Mechanical pressure is converted into hydrostatic pressure by the chamber lid and transmitted to the perovskite, as shown in [Figure 1B](#)<sup>[57]</sup>. To prevent the perovskite from being corroded by the transmitting liquid, they are usually encapsulated in heat-resistant Teflon bags. Additionally, to facilitate better pressure transmission, a hydrophobic, smooth, rigid film, such as a hydrophobic silicon wafer, is typically placed on the surface of the film<sup>[51]</sup>. In some studies, high-pressure gas is also used as the pressure-transmitting medium<sup>[58]</sup>. Although this pressure mode is considered hydrostatic, in practice, the films deposited on rigid substrates mainly experience uniaxial pressure applied along the Z-axis through the covering plate. We believe that in current studies, the pressure applied in the PAC process is mainly uniaxial. Some PAC processes are conducted at room temperature, primarily focusing on the fabrication of thick perovskite wafers for X-ray detectors<sup>[59]</sup>. However, most PAC processes are combined with thermal annealing. In open systems, pressure and heating are combined by applying a heating module to both the sample holder and platen [[Figure 1C](#)]<sup>[60]</sup>. In closed systems, heating can be achieved by applying a thermocouple to the sealed chamber. Since heat is transferred through a liquid medium, this method ensures a more uniform heat distribution. Moreover, the closed system can suppress the thermal decomposition of perovskite materials containing volatile amines, thereby extending the duration of the thermocompression process and better leveraging the advantages of this technique. In addition, nanoimprint technology has also been applied to the recrystallization process of perovskite, typically combining pressure and thermal annealing, which belongs to an open system [[Figure 1D](#)]<sup>[61]</sup>. Through the thermocompression process, substrate-free perovskite wafers, perovskite films on substrates, and even welded perovskite layers can be obtained. However, regardless of the type of thermocompression technology used, the platen (as well as the underlying substrate) in direct contact with the perovskite film significantly impacts the film's interface. Hydrophilic rigid platen tends to adhere

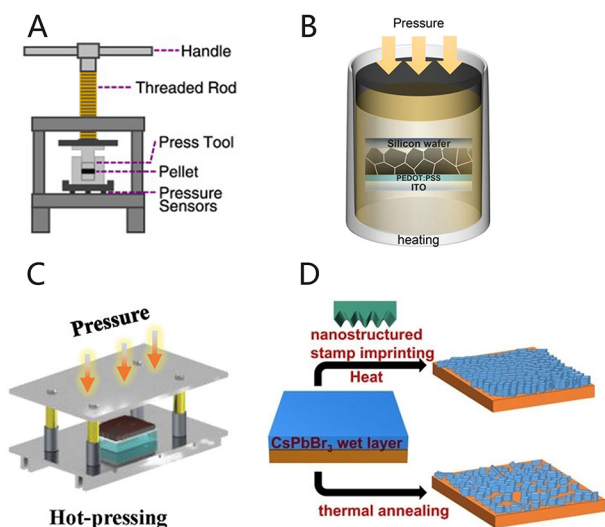


**Figure 1.** Schematic illustration: (A) The open pressure equipment. This figure is quoted with permission from Witt *et al.*<sup>[52]</sup>. (B) The closed pressure equipment. This figure is quoted with permission from Li *et al.*<sup>[57]</sup>. (C) The open pressure equipment with a heating module. This figure is quoted with permission from Li *et al.*<sup>[60]</sup>. (D) The nanoimprint device. This figure is quoted with permission from Zhang *et al.*<sup>[61]</sup>.

strongly to the perovskite after thermocompression, and the removal of the platen after pressure release can cause the perovskite film to fracture. This is why hydrophobic silicon wafers are often used as platens. Additionally, chemical degradation is prone to occur at the contact interface due to the presence of significant gaps, which allow volatile amines in the perovskite material to escape more easily. Moreover, impurities in the film tend to accumulate at the interface due to the pressure-induced “despumption” effect. Therefore, it is essential to use platens (and underlying substrates) with good mechanical properties and low surface roughness. This not only ensures that the platen remains intact under high pressure but also effectively reduces the risk of material degradation.

### Pressure-induced crystallization mechanism

Driven by organic molecule flipping<sup>[62]</sup>, s-p anti-bonding coupling<sup>[63]</sup>, and  $[BX_6]$  octahedral tilt<sup>[64]</sup>, perovskite materials exhibit a characteristic “lattice softness”<sup>[65]</sup>. This softness underpins their unique physical properties, including slow electron-hole recombination, long carrier lifetime, electronic tolerance to defects, *etc.* The softness of perovskite materials also correlates with their low mechanical stiffness and hardness, as evidenced by their low Young's modulus, shear modulus ( $G$ ), and high bulk modulus ( $B$ ). For instance, the  $B/G$  ratio of  $\text{MAPbI}_3$  single crystals reaches 2, exceeding the critical value of 1.75 commonly used to indicate material ductility<sup>[66]</sup>. This indicates that perovskites are ductile materials suitable for both compressive and tensile deformation, forming the basis for pressure-assisted modification.

In crystallization processes assisted solely by pressure, perovskites demonstrate flexible processing characteristics. Li *et al.* ground  $(\text{F-PEA})_3\text{BiI}_6$  single crystals into powder and compressed them under 280 MPa for 5 min to form 2D perovskite wafers<sup>[67]</sup>, as shown in Figure 2A and B. These wafers exhibited pronounced orientation, with resistivity along the vertical direction being four times higher than that in the horizontal direction. X-ray diffraction (XRD) patterns further revealed directional differences: strong diffraction peaks corresponding to  $(0\ 0\ k)$  planes were observed along the Z-axis, while the horizontal diffraction patterns resembled those of powdered samples [Figure 2C]. This anisotropy arises because pressure along the Z-axis compacts the crystal volume, causing the unit cells to align to minimize overall volume. As shown in Figure 2D, when the  $(0\ 0\ k)$  planes are parallel to the substrate, they occupy the least

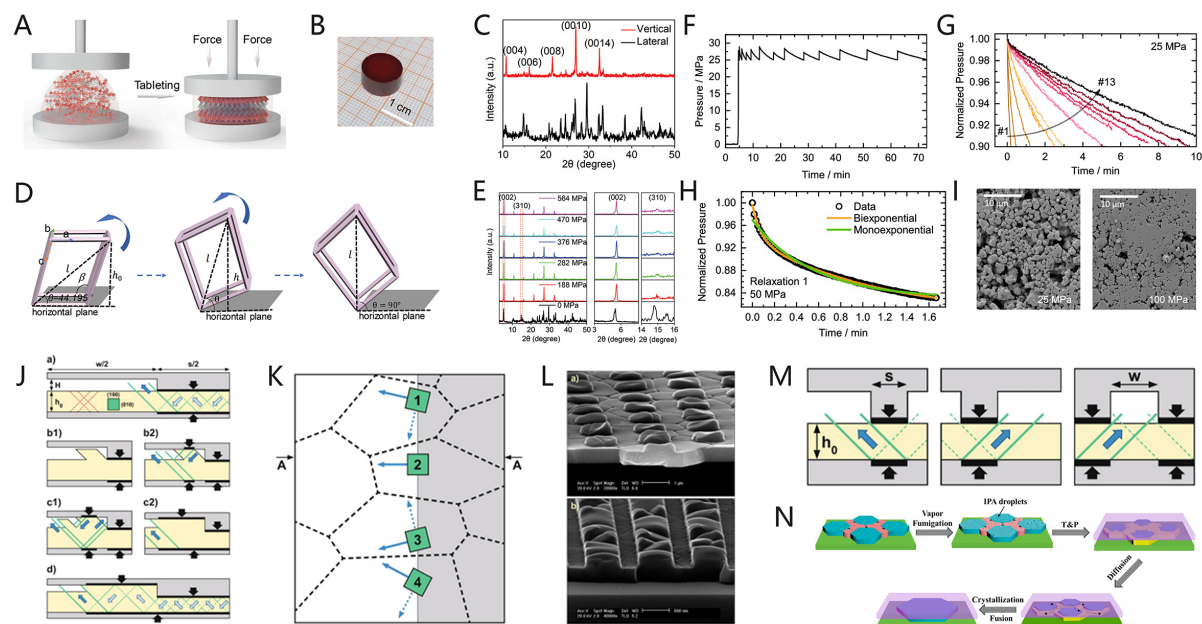


**Figure 2.** (A) Schematic diagram of the tableting principle. (B) The finished (F-PEA)<sub>3</sub>BiI<sub>6</sub> perovskite wafers with a scale bar of 1 cm. (C) XRD patterns showed the layer structure of the cross-section of the 2D (F-PEA)<sub>3</sub>BiI<sub>6</sub> perovskite wafer. (D) Molecular simulations of the tableting process. (E) XRD patterns under different pressures showed the change in diffraction peak intensity of (F-PEA)<sub>3</sub>BiI<sub>6</sub> perovskite wafers including (0 0 2) and (3 1 0) planes. (A-E) are quoted with permission from Li *et al.*<sup>[67]</sup>. (F) Temporal evolution of the applied pressure, during pressing of MAPbI<sub>3</sub> powders at a target pressure of 25 MPa. The pressure was adjusted 13 times manually to keep the target pressure level during the shown time span. (G) Normalized pressure relaxations from (F), with the peak value of the relaxation set as time zero. (H) Normalized first pressure relaxation (black circles), with a target pressure of 50 MPa, together with fits using monoexponential (green) and biexponential (orange) decay. (I) Top view SEM images of the pellets pressed at 25 and 100 MPa. (F-I) is quoted with permission from Witt *et al.*<sup>[68]</sup>. (J) Cartoon to visualize material transport during patterning of a coarse-grained perovskite layer via thermal nanoimprint. (K) Sketch of material transport during the initial phase of imprint with a <1 0 0>-oriented polycrystalline layer. (L) SEM images of MAPbBr<sub>3</sub> processed by nanoimprinting. (M) Sketches indicating alternating material ejection below linear stamp structures. (J-M) is quoted with permission from Mayer *et al.*<sup>[77]</sup>. (N) Schematic illustration of the growth mechanism of the MAPbI<sub>3</sub> film by the PSS strategy. (N) is quoted with permission from Fu *et al.*<sup>[78]</sup>.

vertical space. With increasing pressure, the intensity of the (0 0 k) diffraction peak strengthens, while the intensities of other peaks diminish [Figure 2E]. Witt *et al.* studied the dynamic changes in pressure during compression of nanocrystals<sup>[68]</sup>. Upon applying pressure to MAPbI<sub>3</sub> powder, the volume decreased, and pressure relaxation occurred [Figure 2F]. The relaxation time increased with repeated pressurization cycles [Figure 2G]. This pressure relaxation follows a double exponential decay model<sup>[68]</sup>:

$$P(t) = P_0 + A_1 e^{-t/t_1} + A_2 e^{-t/t_2} \quad (1)$$

where  $A_1, A_2$  are amplitudes, and  $t_1, t_2$  are characteristic relaxation times [Figure 2H]. Two distinct relaxation processes occur: the rearrangement of powder particles and their plastic and elastic deformation. At pressures below 50 MPa, particle rearrangement dominates the compaction process, whereas plastic deformation becomes significant at pressures above 50 MPa. Studies have also shown that under pure pressure conditions, there are noticeable gaps in the pressed perovskite wafers. When the pressure increases, the proportion and size of these gaps are significantly reduced, but they cannot be completely eliminated [Figure 2I]. Furthermore, the wafers retain the morphology of the initial nanocrystals, showing limited grain growth, as confirmed by other studies<sup>[69]</sup>. Mayer *et al.* systematically investigated the grain growth under pressure and concluded that during pressure-assisted crystallization, the thermal component of stress

dominates<sup>[70]</sup>. The total stress  $\sigma$  in perovskite materials can be expressed as:  $\sigma = \sigma_{th} + \sigma_p - \sigma_{gr}$ , where  $\sigma_{th}$  is thermal stress,  $\sigma_p$  is compressive stress under pressure, and  $\sigma_{gr}$  is tensile stress from grain growth. In the early stages of crystal growth,  $\sigma_{gr} \approx 0$ , and total stress is dominated by  $(\sigma_{th} + \sigma_p)$ . As the growth progresses, the driving force for growth from  $(\sigma_p - \sigma_{gr})$  becomes negligible due to the larger  $\sigma_{gr}$ , leaving thermal stress as the main driving force. This explains why pure pressure conditions do not significantly promote grain growth. Given the limited effectiveness of pressure-only methods, most studies focus on combined pressure and thermal treatments. The thermal component provides the necessary energy for further grain growth and activates high-energy grain boundaries. However, for perovskite with volatile amines, annealing may lead to unavoidable decomposition. Pressure-assisted annealing effectively prevents decomposition, allowing the benefits of high-temperature processing<sup>[71]</sup>. Under the combined effect of heat and pressure, more complex crystallization behaviors take place. Polycrystalline films undergo “recrystallization” and “post-crystallization” processes<sup>[72]</sup>. The recrystallization process involves grain re-formation/nucleation for stress relaxation, followed by subsequent grain growth at the cost of other grains. During the grain recrystallization process, excess material is expelled and accumulates at the grain boundaries. At elevated temperatures, a post-crystallization process takes place, during which excess material contributes to the formation of new grains. Regarding the crystal growth behavior under the synergistic effect of pressure and thermal treatments, researchers have varied interpretations. In the classical grain growth theory, the temperature-dominated grain boundary diffusion process leads to a uniform increase in grain size by reducing the system’s interfacial energy, which is a typical characteristic of normal grain growth. Moon *et al.* suggest that the grain regrowth process of perovskite films under the PAC process belongs to abnormal growth, which is mainly attributed to the significant bimodal distribution characteristics of the grains after regrowth<sup>[73]</sup>. This phenomenon arises from the coupling effect of the pressure field and anisotropic crystal growth. Under the constraint of normal pressure, the growth of grains along the film’s normal direction is geometrically restricted, resulting in kinetic advantages for grains with low surface energy orientations such as  $\langle 1\ 0\ 0 \rangle$ . Meanwhile, grain boundary migration parallel to the film surface is significantly enhanced due to the strain energy gradient induced by pressure, promoting the formation of a dominant grain size through directional coarsening of specific grain groups. However, Mayer *et al.* observed that under pressure, the grain growth exponent<sup>[74,75]</sup> for MAPbBr<sub>3</sub> is  $n \approx 3$ <sup>[70]</sup>. This value does not correspond to the conventional exponents for normal growth ( $n = 2$ ) or abnormal growth ( $n = 1$ , characterized by significantly faster than normal growth). Instead, the growth behavior is well described by a capillary-based growth law<sup>[75,76]</sup>.

Furthermore, Mayer *et al.* later applied glide theories from oxide perovskites to explain plastic deformation and void filling in perovskites under pressure<sup>[77]</sup>. Oxide perovskites typically glide along  $\langle 1\ 1\ 0 \rangle$  directions on  $(1\ 1\ 0)$  planes or along  $\langle 1\ 0\ 0 \rangle$  and  $\langle 1\ 1\ 0 \rangle$  directions on  $(1\ 0\ 0)$  planes. Metal halide perovskite crystals exhibit similar properties. For example, in MAPbBr<sub>3</sub>, primary layer grains with preferred  $\langle 1\ 0\ 0 \rangle$  orientation activate  $(1\ 1\ 0)$ - $\langle 1\ 1\ 0 \rangle$  type glide systems under combined pressure and heat. Crystal material is extruded along  $45^\circ$  glide planes to fill cavities, as shown in Figure 2J. The extrusion of top-layer material expands the stressed region and activates additional glide planes, filling smaller residual voids until the cavity is fully compacted. In polycrystalline materials, glide initiates in grains with the highest resolved shear stress on their glide planes [Figure 2K]. Figure 2L presents Scanning Electron Microscopy (SEM) images of nanoimprinted MAPbBr<sub>3</sub>, revealing angular features that confirm angled “ejections” along glide planes under pressure. Figure 2M provides a schematic illustration of this glide process. These findings highlight the potential of perovskite materials for nanoimprinting and open new possibilities for the fabrication of advanced functional devices.

Moreover, some studies amplify the effects of thermocompression by incorporating solvent adsorption in polycrystalline perovskite films. Fu *et al.* achieved large-grained MAPbI<sub>3</sub> films (~18 μm lateral grain size) by allowing the films to absorb isopropanol prior to thermocompression<sup>[78]</sup>. A sealed pressure environment prevents rapid solvent evaporation, slowing crystallization. Solvent vapor surrounds the film, enabling repeated dissolution-recrystallization cycles that repair the film and extend grain growth, as shown in [Figure 2N](#). Overall, the adsorbed solvents and residual solvents, such as DMSO in perovskite films, lower activation energy and enhance ion migration, further highlighting the “soft” and processable nature of perovskite materials.

Despite significant progress, there is no unified understanding of the pressure-assisted recrystallization mechanism in perovskite materials. Even the most convincing theories lack comprehensive observational data. However, nearly all studies agree that the lattice softness of perovskites fundamentally enables their crystallization under pressure-assisted conditions.

## EFFECTS OF PRESSURE-ASSISTED CRYSTALLIZATION

The PAC process leads to significant improvements in the crystallinity of perovskite polycrystals without altering their spatial structure. These improvements manifest in increased grain size, reduced grain boundaries, enhanced film coverage, and improved crystal orientation. Additionally, some studies have utilized the fusion of grains under thermocompression to achieve “welding” between films, an often-overlooked feature of the PAC process. This section describes the effects of the PAC process on perovskite polycrystals from the following five aspects.

### Grain size

Previous studies on metals and conventional semiconductors have shown that the grain size of polycrystalline films typically reaches an upper limit of about 2-3 times the film thickness<sup>[79,80]</sup>. In solution-processed polycrystalline perovskite films, complexities associated with substrates and impurities often constrain grain sizes to the sub-micron scale. However, the PAC technique has demonstrated the ability to overcome these limitations, yielding remarkably large grain sizes in certain studies. As an example, Wang *et al.* employed a pressure-assisted high-temperature solvent-engineering (PTS) strategy to fabricate high-quality MAPbI<sub>3</sub> films on SiO<sub>2</sub>/Si wafers<sup>[81]</sup>, with some lateral grain sizes reaching up to 90 μm. The preparation process involved covering IPA-adsorbed MAPbI<sub>3</sub> films with hydrophobic silicon wafers, wrapping them in Teflon, and placing the assembly in a pressure vessel at 150 °C and 150 MPa, as shown in [Figure 3A](#). The total processing time extended up to 5 h, as the closed chamber suppressed decomposition, providing sufficient treatment time. Under the combined influence of solvent, pressure, and heat, the original films underwent significant grain growth [[Figure 3B](#)]. The resulting films achieved an average lateral grain size of 49.8 μm, dramatically larger than the conventional annealing (CA) film of 0.41 μm, despite a film thickness of only 580 nm [[Figure 3C-E](#)]. The defect density was reduced to  $7.43 \times 10^{11} \text{ cm}^{-3}$ , slightly higher than that of single-crystal MAPbI<sub>3</sub> but 63 times lower than the original film's defect density of  $4.7 \times 10^{13} \text{ cm}^{-3}$ . This substantial reduction in defect concentration extended the slow decay component of time-resolved Photoluminescence (PL) to the microsecond scale [[Figure 3F](#)]. Zhang *et al.* prepared high-quality dual-cation FA<sub>0.2</sub>MA<sub>0.8</sub>PbI<sub>3</sub> films using similar equipment<sup>[82]</sup>. The obtained films demonstrated grain sizes exceeding the original films, with average grain sizes of 5 μm on solution-processed SnO<sub>2</sub> layers [[Figure 3G](#)]. Regardless of thickness (ranging from 109 nm to 1.5 μm), individual grains extended vertically across the films, as shown in [Figure 3H](#). The XRD patterns further confirmed a notable enhancement in crystallinity, with a significant increase in diffraction intensity [[Figure 3I](#)]. At the same time, no new diffraction peaks appeared, indicating a uniform distribution of FA<sup>+</sup> and MA<sup>+</sup> ions. Interestingly, in certain cases, PAC can induce phase separation in multi-cation films, a phenomenon discussed later.

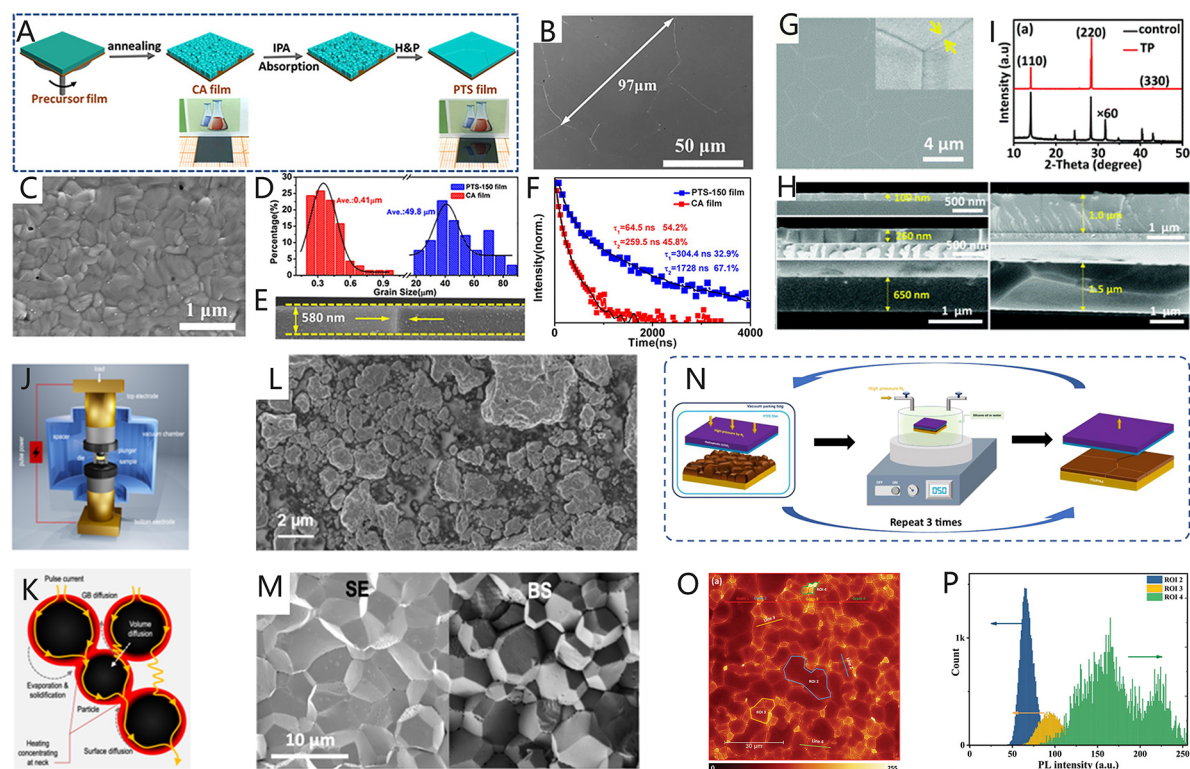


**Figure 3.** (A) Schematic illustration of the PTS process for the fabrication of the  $\text{MAPbI}_3$  film. Top-view SEM images of the (B) PTS-150 film and (C) CA film. (D) Grain size distribution of the PTS-150 film and CA film. (E) Cross-sectional SEM image of the PTS-150 film. (F) Time-resolved PL spectra of PTS-150 and CA films. (A-F) is quoted with permission from Wang *et al.*<sup>[81]</sup>. (G) Top-view SEM image of  $\text{SnO}_2$ -TP75 film. (H) Cross-sectional SEM images of  $\text{SnO}_2$ -TP75 film of different thicknesses. (I) XRD patterns of control and TP films. (G-I) is quoted with permission from Zhang *et al.*<sup>[82]</sup>. (J) Setup configuration of FAST. (K) Mass transport mechanisms involved in the sintering, including volume diffusion, evaporation and solidification, grain boundary diffusion, and surface diffusion. (L) The as-milled  $\text{MAPbI}_3$  powders. (M) The cross-section SEM image of the FAST-synthesized  $\text{MAPbI}_3$  bulk. (J-M) is quoted with permission from Zheng *et al.*<sup>[83]</sup>. (N) Schematic diagram of the preparation process for the CHC-treated perovskite film. (O) CLFM image of the ETL/CHC-treated perovskite film/HTL film. (P) Statistical histograms of PL intensities in areas ROI2, ROI3, and ROI4 of (O). (N-P) is quoted with permission from Zhang *et al.*<sup>[84]</sup>.

Furthermore, Zheng *et al.* introduced an electrical and mechanical field-assisted sintering technique (EM-FAST), which is different from conventional heating using electric couples<sup>[83]</sup>. This method combines pressure equipment with a high-power electrical circuit within a controlled atmosphere [Figure 3J]. By applying a low voltage yet high pulse current (1-10 kA), sufficient Joule heating is generated, rapidly elevating the temperature to a high level within 10 mins. During this process, the current flows through both the die and the sample. Perovskite powder is directly placed in a mold, and as compressive pressure (~50 MPa) is applied, the pulse current passes through the sample, concentrating heat at the particle necks, which triggers mass transfer and grain merging between adjacent powders [Figure 3K]. This technique enables rapid grain coarsening of polycrystalline perovskite, producing  $\text{MAPbI}_3$  bulk crystals with a diameter of 12.7 cm and a thickness of approximately 0.2 cm. The resulting grains exhibit a highly dense structure with a regular polygonal morphology and an average size of ~7  $\mu\text{m}$ , which stands in stark contrast to the initial film [Figure 3L and M]. According to single-carrier device estimates, the defect density of these crystals is  $5.4 \times 10^{10} \text{ cm}^{-3}$ , while the hole mobility reaches  $1.7 \text{ cm}^2 \text{ V}^{-1} \text{ s}^{-1}$ , which is exceptional performance for this size.

Based on the PAC technique, Zhang *et al.* proposed a new perspective on grain size [Figure 3N]<sup>[84]</sup>. They achieved the  $\text{FA}_{0.83}\text{Cs}_{0.07}\text{MA}_{0.13}\text{PbI}_{2.64}\text{Br}_{0.39}$  film with an average grain size of  $7.14 \pm 3.68 \mu\text{m}$  using high-pressure gas as the pressure medium. Through confocal laser scanning fluorescence microscopy (CLFM), they observed a grain size-dependent PL intensity in the perovskite/transport composite film [Figure 3O and P]. When the grain size was smaller than  $10 \mu\text{m}$ , PL intensity was inversely proportional to grain size, suggesting that larger grains were more severely quenched by the transport layer. However, when the grain size exceeded  $10 \mu\text{m}$ , the PL intensity stabilized, indicating that photogenerated carriers achieve the optimal transport rate only when the grain size surpasses  $10 \mu\text{m}$ . This challenges the conventional belief that the most efficient photoinduced charge transfer occurs when the grain size exceeds the film thickness<sup>[41]</sup>. It underscores the importance of the PAC technique for its ability to bring the grain size closer to the point where all grains exceed  $10 \mu\text{m}$ .

In the aforementioned studies, perovskite films with enlarged grains demonstrated a substantial reduction in defect density compared to their as-prepared counterparts. This enhancement primarily originates from a pressure-thermal synergistic restructuring mechanism. Under optimized pressure-temperature conditions, the cooperative energy input enables atomic rearrangement by providing sufficient activation energy to overcome diffusion barriers<sup>[73,83]</sup>, thereby driving structural reorganization at multiple scales<sup>[85,86]</sup>. At the macroscopic scale, this phenomenon manifests as the synergistic evolution of grain coarsening, grain boundary annihilation, and pore elimination. At the atomic level, it is characterized by a significant suppression of defects, which is evidenced by a notable extension in the fluorescence lifetime associated with intra-grain radiative recombination<sup>[78,81]</sup>. The low-defect nature of these perovskite films profoundly enhances the performance of functional devices. The marked reduction in defect density effectively suppresses non-radiative recombination, leading to significantly improved photoelectric conversion efficiency in optoelectronic devices. Furthermore, the reduced defect density improves carrier mobility and lifetime, which is critical for high-performance photodetectors<sup>[87]</sup>. Additionally, defect suppression enhances material stability by mitigating ion migration and phase segregation, thereby extending device operational lifetimes. In LEDs, lower defect densities promote radiative recombination efficiency, enabling higher external quantum efficiency and purer emission spectra. Collectively, the pressure-thermal synergistic restructuring mechanism enables the fabrication of low-defect perovskite films, laying a solid foundation for developing efficient, stable, and multifunctional devices.

### Grain boundary

Grain boundaries, which are rich in defects, significantly degrade the performance and stability of perovskite crystals. In recent years, extensive studies have shed light on the detrimental effects of grain boundaries<sup>[88,89]</sup>, so we will not delve into those details here. In pressure-assisted thermal treatment studies, a remarkable reduction in grain boundaries is observed, particularly in the direction of the applied pressure, where they almost completely disappear. This phenomenon occurs during both the recrystallization process, where grains with lower surface energy grow by consuming those with higher surface energy, and the post-crystallization process, where excess material accumulates at grain boundaries to form new grains. Even under relatively low additional pressure ( $4,900 \text{ Pa}$ ), the synergistic effect of heat can effectively reduce grain boundaries in polycrystalline thin films. Luo *et al.* demonstrated that by simply placing weights on top of the film during annealing, they achieved a significant reduction in grain boundaries [Figure 4A-D], effectively enhancing the optoelectronic performance and environmental stability<sup>[90]</sup>. Notably, during pressure-assisted thermal treatment, the mobility of grain boundaries is driven by heat, while pressure provides the driving force for secondary grain growth. Other research has suggested an alternative perspective, proposing that the primary role of pressure is to maximize thermal stress, which dominates grain growth by preventing sample bending<sup>[70]</sup>. This explains why pressing at room temperature, even at high pressures, cannot eliminate grain boundaries, while at elevated temperatures, even low pressure can

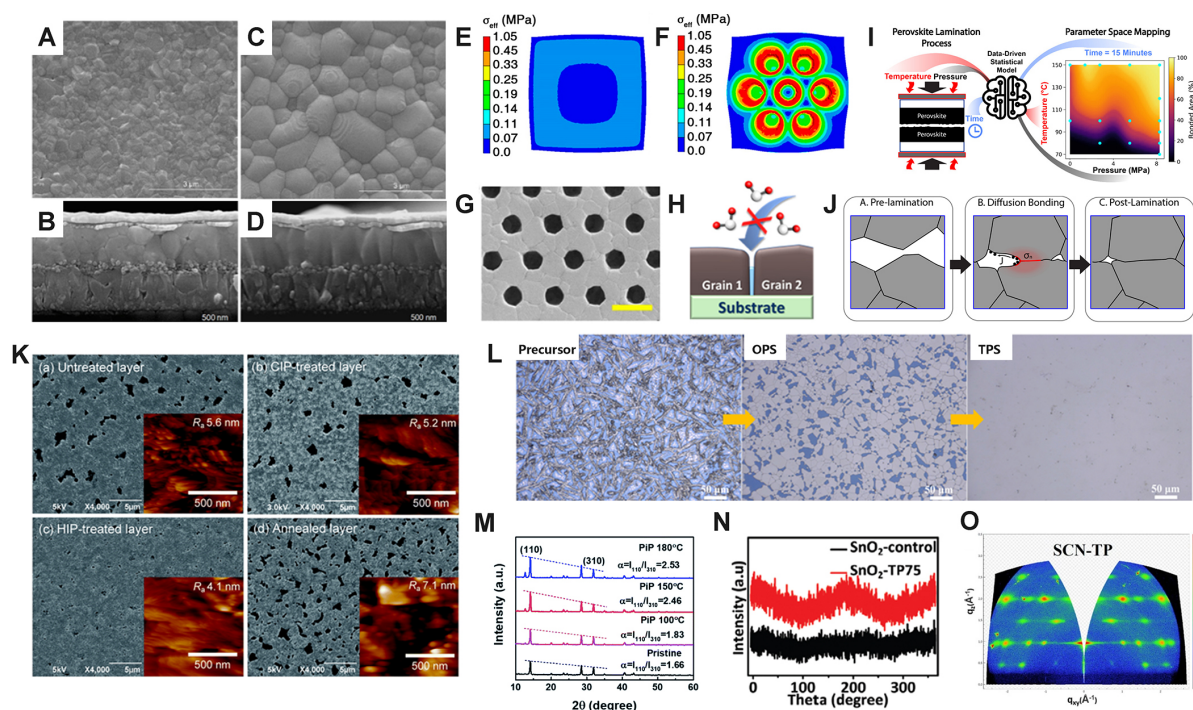


**Figure 4.** The top-view SEM images of the (A) conventional and (C) PASP perovskite films with pressure of 4,900 Pa. Cross-sectional SEM images of the (B) conventional and (D) PASP perovskite films with an additional pressure of 4,900 Pa. (A-D) is quoted with permission from Luo *et al.*<sup>[90]</sup> The mechanical simulation of (E) fp- and (F) hp-OIHP films. (G) The top-view SEM images of hp-OIHP film. (H) Schematic diagram of grain boundaries. (I and J) is quoted with permission from Lanaghan *et al.*<sup>[92]</sup> (K) SEM images of untreated, CIP-treated, HIP-treated, and annealed perovskite layers. (K) is quoted with permission from Matsushima *et al.*<sup>[69]</sup> (L) Optical images of perovskite precursor, OPS, and TPS films. (L) is quoted with permission from Wang *et al.*<sup>[95]</sup> (M) XRD patterns of pristine and PIP perovskite films with diverse temperatures. (M) is quoted with permission from Huang *et al.*<sup>[96]</sup> (N) Phi-scan patterns of SnO<sub>2</sub>-control and SnO<sub>2</sub>-TP films. (N) is quoted with permission from Zhang *et al.*<sup>[82]</sup> (O) GIWAXS images of SCN-TP film. (O) is quoted with permission from Zhu *et al.*<sup>[51]</sup>

promote substantial grain growth. Moreover, research suggests that the purity of the starting materials strongly influences grain boundary mobility, with high-purity materials imparting higher mobility to grain boundaries<sup>[77]</sup>.

Additionally, Chun *et al.* introduced a new perspective on grain boundary research in pressure-thermal-assisted polycrystalline perovskite materials<sup>[91]</sup>. They applied a uniaxial compression force of 0.14 MPa at 100 °C to perovskite films using a polyurethane (PUA) stamp with a hexagonal nanopattern array. Unlike flat pattern (fp-) stamping, the hexagonal dot pattern (hp-) stamp generated a more complex stress environment for the perovskite films [Figure 4E and F]. It induced axial deformation while simultaneously creating lateral tensile deformation in each nanodot pattern along the X and Y directions. Polycrystalline films situated between the nanodot patterns experienced localized multiaxial compressive stress. Consequently, the synthesized compressive stress was higher than that achieved with planar stamping, ultimately yielding high-quality polycrystalline films with low-angle grain boundaries, as shown in Figure 4G. Low-angle grain boundaries have minimal defects and can resist the erosion of water vapor, offering better stability [Figure 4H]. This will significantly improve the quality of the polycrystalline film, bringing it closer to the properties of a single crystal.

It is noteworthy that, based on the phenomenon of grain boundary elimination and grain fusion under normal pressure, researchers have developed a novel method for fabricating layered devices by “welding” different perovskite films together using applied pressure. Lanaghan *et al.* investigated the process-structure relationships during the lamination of  $\text{FA}_{0.8}\text{MA}_{0.15}\text{Cs}_{0.05}\text{PbI}_{2.6}\text{Br}_{0.4}$  films [Figure 4I]<sup>[92]</sup>. During this lamination process, two independent perovskite films underwent “diffusion bonding”. The applied pressure and thermal treatment induced elastic and plastic deformation of the film surfaces, forming tight contact between them. This mechanical deformation was coupled with the diffusion of atomic or molecular species along and across the bonding interface. As a result, chemical bonds formed at the interface, as illustrated in Figure 4J. The study revealed that the percent bonded area (PBA) depended on both the applied pressure and temperature. At relatively low pressures (2 MPa), higher temperatures (e.g., 150 °C) were sufficient to achieve a larger PBA. Even at the highest pressure tested (8 MPa), the PBA increased monotonically with temperature. This suggests that increasing pressure is more effective at lower temperatures, while at higher temperatures, faster diffusion reduces the relative importance of pressure. These findings underscore the critical role of temperature in the PAC process. Under the same pressure, solar cells fabricated at higher temperatures exhibited superior performance, particularly in current parameters, due to the larger effective area created by improved bonding. Additionally, Yang *et al.* achieved perovskite laminates with dual flexible substrates by hot-pressing two independently fabricated  $\text{CsPbBr}_3$  films on flexible polyethylene terephthalate (PET)<sup>[93]</sup>. The composite film, formed at 90 °C and 10 MPa, demonstrated impressive mechanical strength, withstanding horizontal pulling pressures of 636 kPa and vertical pulling pressures of 71 kPa. This work highlights a promising approach to physically laminating perovskite films, potentially accelerating the development of roll-to-roll printed perovskite devices and perovskite tandem architectures. Lamination processes address some of the fabrication challenges in perovskite devices, such as the inability to deposit other perovskite materials onto pre-formed films due to solvent compatibility issues, and the difficulty of depositing transparent metal oxides as the top electron. Furthermore, lamination enables the fabrication of thicker perovskite films, overcoming solubility limitations. This technique broadens the applications of thermocompression treatments and redefines the conventional bottom-up processing sequence used in solution-based methods.

### Film coverage

Conventional preparation methods aimed at promoting grain growth typically do not eliminate the gaps in polycrystalline films, as these regions lack sufficient material to support grain growth and are difficult to fill. The rapid crystallization method is effective for preparing dense films, but the film’s density is achieved by the anti-solvent, which restricts further grain growth<sup>[94]</sup>. In the pressure- and heat-assisted crystallization process, pressure not only drives secondary crystal growth but also forces the perovskite material into the voids<sup>[77]</sup>. The resulting films and wafers exhibit significant densification while the grains grow sufficiently, which is a distinctive feature of the thermocompression treatment. Matsushima *et al.* conducted a systematic study on the changes in film coverage caused by the PAC process<sup>[69]</sup>. Their experimental results showed that, compared to the initial film coverage (93.7%), cold isostatic pressing (200 MPa; room temperature) did not significantly improve the coverage. However, when both pressure and heat were applied (200 MPa; 90 °C), the film coverage increased significantly (to 98.1%). Films that underwent only the annealing process showed a decrease in coverage (to 86.5%). The SEM images of these four types of thin films provide an intuitive comparison [Figure 4K]. The hot-pressed films exhibited the best electron and hole diffusion distances, effectively enhancing the photovoltaic performance of solar cells based on these films.

It is worth noting that Wang *et al.* have made notable contributions to improving film coverage through pressure-assisted heat treatment<sup>[95]</sup>. They employed a two-round pressure-assisted solvent-engineering (TPS) strategy to obtain a dense film, using a  $\text{MAPbI}_3$  dendrite film with low coverage as the template. From

the precursor film to the OPS film (processed once), and then to the TPS film (processed twice), the film coverage progressively increased, with the final film showing almost no visible gaps [Figure 4L]. This post-treatment method significantly reduced the preparation requirements for the original film and provided valuable insights into processing films with low coverage and minimal pinholes.

### Crystal orientation

In the PAC process, due to the compressive stress along the Z-axis direction in the geometric space, perovskite grains are guided to form a preferred orientation, minimizing both elastic and surface energy. Significant improvements in the grain orientation of polycrystalline films have been observed in many studies on the PAC process. Huang *et al.* observed crystallization orientation changes with temperature during the PAC process of MAPbI<sub>3</sub> film<sup>[96]</sup>. As the temperature increased, the intensity ratio between the (1 0 0) and (3 1 0) planes gradually increased, indicating the crystal tends to grow preferentially along the (1 0 0) direction [Figure 4M]. Zhang *et al.* investigated the crystallographic properties of FA<sub>0.2</sub>MA<sub>0.8</sub>PbI<sub>3</sub> films after thermocompression treatment (75 MPa; 100 °C) using phi-scan measurements<sup>[82]</sup>. They found that the phi-scan of the (1 1 0) plane exhibited two peaks separated by 180°, while no clear peaks were observed in the curve of the disordered control film, demonstrating the high degree of orientation in the hot-pressed film [Figure 4N]. Zhu *et al.* employed the PAC process to enhance the crystallization orientation of 2D-3D perovskite films<sup>[51]</sup>. The structural orientation of the films was further analyzed using grazing-incidence wide-angle X-ray scattering (GIWAXS). The 2D scattering pattern of the control film displayed typical diffraction rings, whereas for the PAC-treated film (SCN-TP film), distortion and elongation of the diffraction points were greatly reduced, and the orientation of the structure was significantly improved, as shown in Figure 4O.

## DEVICE APPLICATION

### Solar cell

The performance of perovskite solar cells is closely linked to the crystallinity of the perovskite active layer. The significant improvement in crystallinity achieved through PAC treatment can effectively enhance both the photovoltaic performance and stability of perovskite solar cells. The application of the PAC process in perovskite solar cells dates back to 2015, when Matsushima *et al.* first investigated the effects of pressure and the synergistic influence of pressure and heat on MAPbI<sub>3</sub> films<sup>[69]</sup>. At that time, perovskite solar cell was still in its early stages, and devices fabricated using thermocompression treatment only achieved an average efficiency of 10.6%. However, compared to untreated devices, the efficiency improved by 47%, and the films exhibited clear signs of densification and enhanced crystallinity. Two years later, Chen *et al.* proposed a method for fabricating large-area perovskite solar cells based on pressure treatment<sup>[97]</sup>. As shown in Figure 5A, this method utilizes amine complexes (CH<sub>3</sub>NH<sub>2</sub>·mCH<sub>3</sub>NH<sub>2</sub> and PbI<sub>2</sub>·nCH<sub>3</sub>NH<sub>2</sub>) as precursors. Under pressure (120 bar), the precursors are spread on the substrate and covered with a polyimide (PI) film. The thin liquid film is then heated at 50 °C for 2 min. After peeling off the PI film, a dense and uniform MAPbI<sub>3</sub> film is formed. The resulting films exhibited significantly larger grain sizes compared to those prepared by spin-coating [Figure 5B]. Small-area devices (1 cm<sup>2</sup>) based on this film achieved an efficiency of 19.3%. This method also proves to be suitable for the fabrication of large-area devices, as it can quickly form perovskite films with an area of approximately 60 cm<sup>2</sup>, and small modules (36.1 cm<sup>2</sup>) based on these films achieved 13.9% efficiency [Figure 5C]. This was an important attempt to prepare large-area devices in the early development of perovskite solar cells.

In 2021, Huang *et al.* promoted the recrystallization of perovskite films using a planar imprint (PiP) method. During this process, trimethoxy (1H,1H,2H,2H-heptadecafluorodecyl) silane (FAS) oligomers were transferred to the surface of the perovskite films to passivate defects<sup>[96]</sup>. As shown in Figure 5D, a silicon wafer coated with FAS oligomers was placed on top of the MAPbI<sub>3</sub> film, and a platen applied 3 MPa of

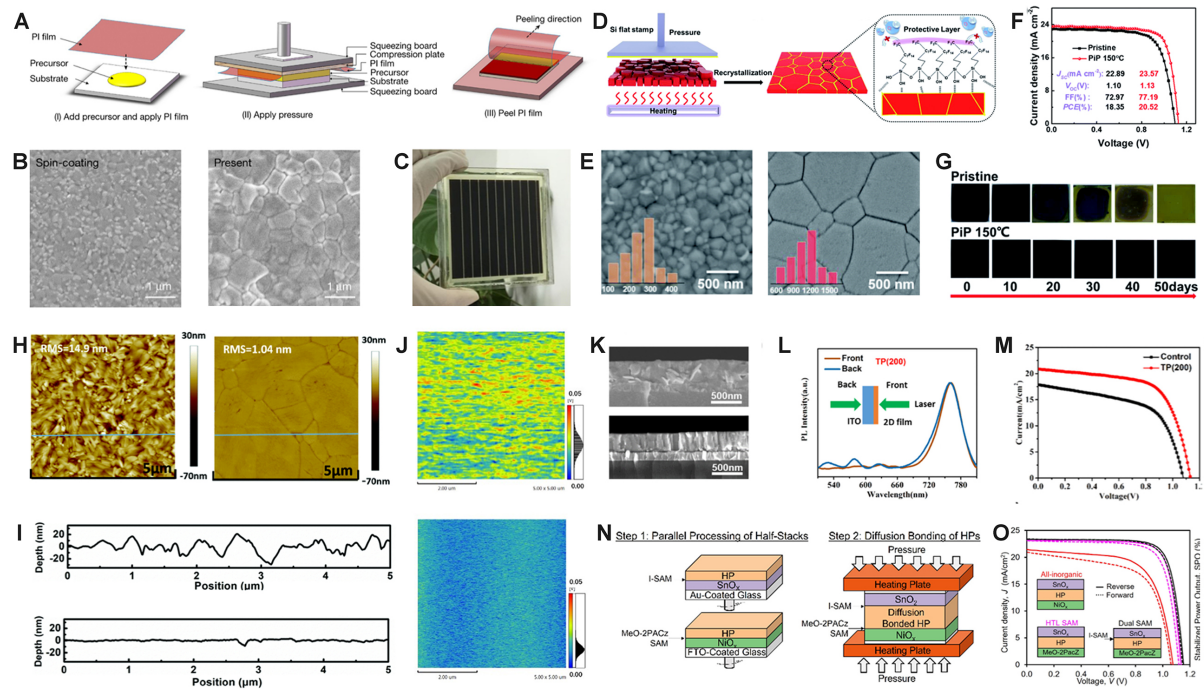


**Figure 5.** (A) The steps of the pressure processing method. (B) Top-view SEM images of the perovskite film via the pressure processing method and a reference sample using the spin-coating method. (C) Photograph of a module. (A–C) is quoted with permission from Chen *et al.*<sup>[97]</sup>. (D) The schematic diagram of the PIP process introduced FAS oligomer barrier to resist moisture. (E) The top-view SEM images of pristine and PIP 150 °C films. (F) *J*-*V* curves of pristine and PIP 150 °C films. (G) Pictures of fresh and aged pristine and PIP 150 °C films. (D–G) is quoted with permission from Huang *et al.*<sup>[96]</sup>. (H) AFM topographic images, (I) surface profile of the precursor film and the TPR film. (J) KPFM image of Au electrode based on control film and TPR film. (H–J) is quoted with permission from Yu *et al.*<sup>[98]</sup>. (K) Cross-sectional SEM images of control and TP(200) films. (L) PL spectra of the TP(200) film under different excitations. (M) *J*-*V* curves for control- and TP-based devices. (K–M) is quoted with permission from Zhu *et al.*<sup>[100]</sup>. (N) Schematic illustration of the lamination process. (O) *J*-*V* curves in reverse and forward scans for champion devices with different configurations. (N and O) is quoted with permission from Yadavalli *et al.*<sup>[103]</sup>.

pressure through the silicon wafer to the perovskite film, while simultaneously annealing the film. The optimal annealing temperature was 150 °C. After thermocompression treatment, the crystallinity of the film improved significantly, with a noticeable increase in grain size [Figure 5E]. Moreover, the FAS oligomers transferred to the film surface during the imprinting process accumulated at the grain boundaries. These oligomers not only passivated defects but also improved the stability of the grains under moisture. Thanks to these improvements, the optimized devices achieved a maximum PCE of 20.52%, with significantly enhanced stability [Figure 5F and G]. In the same year, Yu *et al.* reported a semitransparent solar cell capable of bidirectional power generation based on the thermal-pressed recrystallizing (TPR) method<sup>[98]</sup>. After the TPR treatment, the perovskite films exhibited remarkable growth, with the average grain size increasing from 340 nm to 1.47 μm [Figure 5H]. Additionally, the hot-pressed film exhibited an exceptionally flat surface, owing to the rigid compression applied, with surface undulations within a few nanometers, as shown in Figure 5I. This was highly favorable for the deposition of ultrathin metallic semitransparent electrodes, which typically have a thickness of less than 20 nm. In contrast, the surface undulations of the control film reached several tens of nanometers, making it clearly unsuitable for the deposition of such thin electrodes. Kelvin probe force microscopy (KPFM) images revealed that the ultrathin Au electrodes deposited on the TPR films had uniform surface potentials, while the control group showed significant fluctuations [Figure 5]. The improvements in active layer crystallinity and electrode conductivity significantly enhanced the all-round performance of the semitransparent solar cells. This work

fully harnessed the synergistic effects of pressure and heat, providing a novel approach for the fabrication of semitransparent solar cells with ultrathin perovskite films and electrodes.

In 2022, Zhang *et al.* reported the application of the PAC process in ternary cation perovskite materials<sup>[99]</sup>. They employed relatively mild hot-pressing conditions (8 MPa; 50 °C). After the PAC process, the grain size of the film increased significantly, with the average grain size growing from 0.16 to 3.30 μm. The best efficiency of the solar cell based on this film reached 23.07%, compared to only 20.02% for the control devices. Furthermore, the optimized devices exhibited better resistance to halide movement and photochemical decomposition, maintaining 85% of their initial efficiency after 60 days of ambient exposure, while the control group only retained 50%. Shortly thereafter, Zhu *et al.* used the hot-press effect to achieve substantial control over the quality of quasi-2D perovskite films<sup>[100]</sup>. After treatment under 200 MPa pressure at 100 °C, the quasi-2D films (PEA<sub>2</sub>MA<sub>4</sub>Pb<sub>5</sub>I<sub>6</sub>) recrystallized into a stripe structure perpendicular to the substrate, which enhanced charge transport. In contrast, untreated films exhibited randomly oriented grains on the substrate [Figure 5K]. The phase composition and distribution of 2D Ruddlesden-Popper perovskite films are crucial for charge transfer through the vertically oriented structures. The hot-pressed films exhibited a relatively pure  $n = 5$  phase, while lower  $n$ -phase materials were primarily located at the bottom near the substrate, as confirmed by PL spectra obtained from the films excited at different incident angles [Figure 5L]. This arrangement forms an energy funnel that facilitates charge transfer between different phases, making it particularly suitable for inverted structure perovskite solar cells. This study provided evidence that pressure can also be used to control the phase distribution within the films. Thanks to the reduced defect density and enhanced carrier transport induced by the hot-pressing process, the device efficiency improved significantly from 11.10% to 15.14% [Figure 5M]. This work demonstrates the versatility of the hot-press process across various perovskite materials and highlights its potential to provide additional control over 2D perovskite materials.

Moreover, Li *et al.* successfully fabricated bifacial perovskite solar cells with bidirectional power generation capability using thermal lamination technology<sup>[101]</sup>. They employed a highly conductive adhesive (d-sorbitol) as an intermediate layer, achieving effective bonding between ITO conductive films and perovskite composite layers under conditions of 100 °C and 2,000 psi pressure within just 45 s. Experimental results demonstrated that the dual-ITO-electrode device exhibited exceptional stability and achieved a bifaciality factor of 0.93, comparable to commercial silicon-based solar cells. This study validates thermal lamination as a simplified alternative bonding mechanism for optimizing device architectures, provides critical insights into the application of lamination technology in perovskite photovoltaics, and has spurred a series of subsequent related investigations in this field<sup>[102]</sup>. Subsequently, in early 2024, Yadavalli *et al.* reported an updated lamination process for perovskite solar cells, applying 5.7 MPa of pressure at 150 °C to bond two face-to-face independent half-stacks<sup>[103]</sup>, thereby forming a complete solar cell [Figure 5N]. The laminated films had a thickness twice that of the original films, and the grain size was significantly increased. Devices based on these films achieved an efficiency of 21.0%, which is the highest efficiency obtained by the lamination process to date [Figure 5O]. Additionally, the devices featured a fully inorganic transport layer structure, which could not be achieved by the conventional bottom-up spin-coating method. This structure contributes to both improved stability and reduced cost. The study also highlighted the critical role of functionalized self-assembled monolayers in enhancing interface performance during the lamination process. This work addresses many limitations of traditional solution-processed solar cells and provides valuable insights for developing high-stability, low-cost perovskite solar cells. However, the performance of photovoltaic devices based on lamination processes is still relatively low. The fundamental reason is that the perovskite thin films, with sub-micron thickness, experience incomplete bonding during the lamination process due to uneven stress, which is caused by the interface irregularities from solution-based

crystallization. To address this issue, the application of thermally meltable conductive polymers in the lamination process could be a potential way to improve the lamination quality.

### Photodetector

Similar to perovskite solar cells, perovskite photodetectors, which are also based on the material's optoelectronic properties, are profoundly influenced by the PAC technique. This technique not only enhances the photocurrent of the photodetector, but also has a positive impact on its responsivity, dark current, response time, and linear dynamic range (LDR), among others.

In 2018, Dong *et al.* employed a solvent-assisted thermal pressure (ST) strategy to promote secondary grain growth, resulting in enhanced crystallinity in  $\text{CH}_3\text{NH}_3\text{PbI}_{3-x}\text{Cl}_x$  perovskite films<sup>[104]</sup>. The ST process effectively improved the film quality, including grain enlargement and the elimination of grain boundaries [Figure 6A]. Lateral photodetectors based on ST-treated films demonstrated excellent detection performance, with clear responses to light at wavelengths of 405, 465, 532, and 671 nm. Compared to conventional annealed (CA) film devices, the photodetectors based on ST films showed significant improvements in photocurrent, increasing from 6.4 to 83  $\mu\text{A}$  under 20.6  $\text{mW}/\text{cm}^2$  illumination at 671 nm, achieving an ultra-high on/off ratio of  $2.1 \times 10^4$  at a 10 V bias [Figure 6B and C]. The photocurrent remained stable during on/off cycles, with no significant variation in signal amplitude, indicating good reversibility and stability. Additionally, the ST film devices exhibited fast switching, with rise and decay times of 54 and 63  $\mu\text{s}$ , as shown in Figure 6D. In the same year, Zhou *et al.* employed a pressure-assisted annealing (PAA) strategy to fabricate self-driven photodetectors based on  $\text{CsPbBr}_3$  microcrystals<sup>[105]</sup>. When the film thickness exceeded the size of the  $\text{CsPbBr}_3$  microcrystals, high-density voids and rough surfaces formed, greatly limiting the application of  $\text{CsPbBr}_3$  microcrystals in photodetector devices. In this study, PAA treatment (7.5 MPa; 150 °C) effectively reduced the void density within the microcrystal films and provided a smooth surface [Figure 6E and F], facilitating subsequent functional layer deposition. The self-driven photodetectors based on the PAA films exhibited performance that was directly related to the applied pressure. As pressure increased, the dark current density ( $J_{\text{dark}}$ ) decreased exponentially, while the photocurrent density ( $J_{\text{ph}}$ ) increased exponentially, resulting in an increased on/off ratio [Figure 6G]. The best detection performance was achieved at 7.5 MPa pressure. When illuminated with 473 nm light, the current density increased linearly from 2.5  $\text{nA}/\text{cm}^2$  to a maximum of 3.8  $\text{mA}/\text{cm}^2$  as the light power varied from  $6.4 \times 10^{-6}$  to 0.64  $\text{W}/\text{cm}^2$ , resulting in a LDR of up to 123.5 dB [Figure 6H]. Moreover, the device's responsivity remained nearly constant within the linear response range, reaching 2.06  $\text{A}/\text{W}$ . In contrast, the reference device without pressure treatment, due to the presence of significant voids, exhibited a high dark current density of 0.42  $\mu\text{A}/\text{cm}^2$  and a small photocurrent density of 3.2  $\mu\text{A}/\text{cm}^2$  at -0.05 V when illuminated with a 473 nm laser (0.64  $\text{mW}/\text{cm}^2$ ).

In 2021, Shang *et al.* reported a solvent-assisted thermal-pressed (STP) method to induce phase separation in binary cation perovskite ( $\text{FA}_{0.1}\text{MA}_{0.9}\text{PbI}_3$ ) films<sup>[106]</sup>. The STP process involved placing the precursor film, adsorbed with IPA vapor, into a sealed autoclave, where pressure and temperature (100 MPa; 100 °C) were applied via simethicone. After STP treatment, the films exhibited tightly packed micron-sized grains, contrasting sharply with the dendritic precursor films and significant voids, greatly improving their detection performance. Notably, phase separation was observed in the film, with particles that were distinctly darker than the surrounding regions [Figure 6I]. These particles, confirmed by PL spectra and XRD patterns [Figure 6J], were identified as independent  $\delta$ -FAPbI<sub>3</sub> grains. This phenomenon contrasts with previous reports where PAC treatment resulted in a uniform distribution of multications within the film. The authors attributed this effect to the differing ionic radii of  $\text{MA}^+$  and  $\text{FA}^+$ , with the pressure-induced “despumatation” effect promoting the migration of doped  $\text{FA}^+$  ions from the bulk to the grain boundaries, where they recrystallized.  $\delta$ -FAPbI<sub>3</sub> has stable chemical properties, can passivate defects, inhibit cation

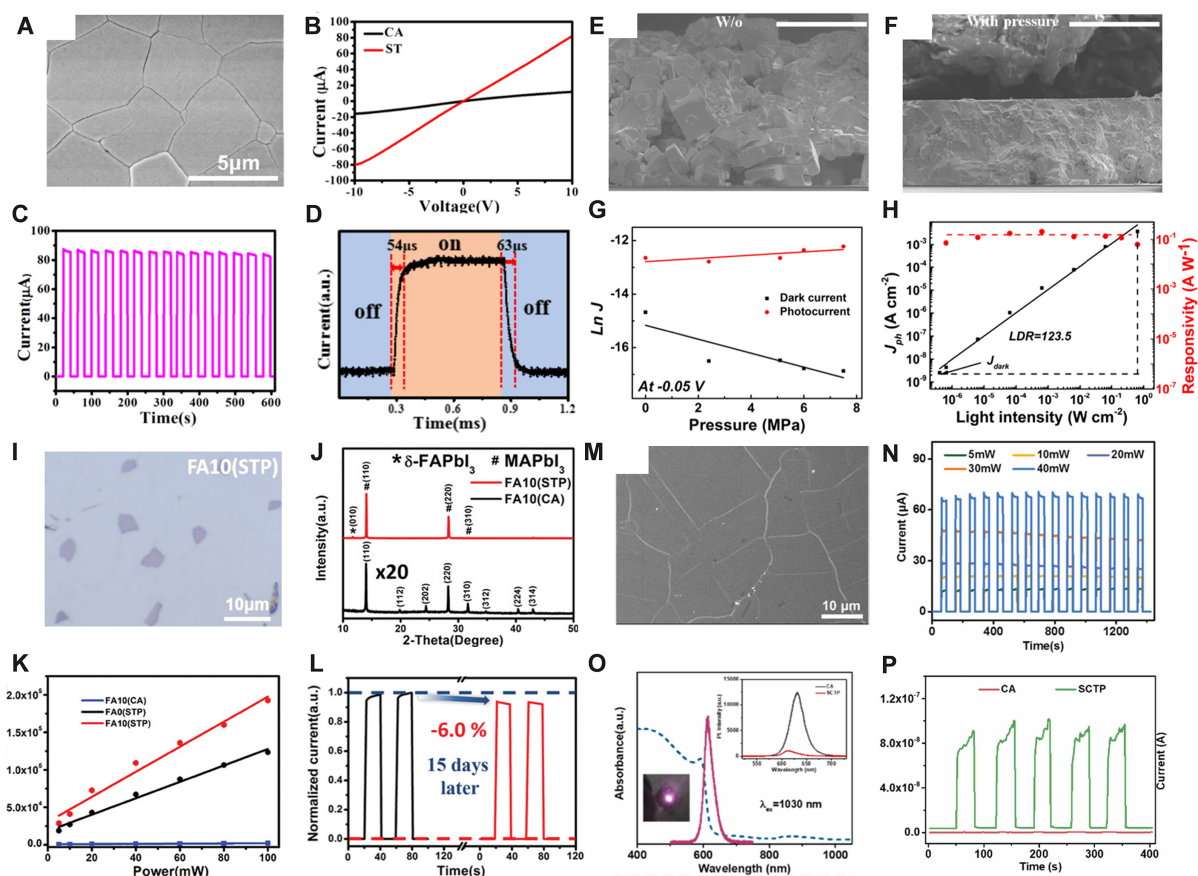


**Figure 6.** (A) Top-view SEM image of the ST perovskite film. (B) I-V curves of photodetectors with CA and ST films for 671 nm laser under  $20.6 \text{ mW/cm}^2$ . (C) Reproducible on/off switching and (D) transient photocurrent (current-time curve) of the ST film photodetector. (A-D) is quoted with permission from Dong *et al.*<sup>[104]</sup> Cross-sectional SEM images of CsPbBr<sub>3</sub> MC perovskite films without (E) and with (F) PAA. (G) Dark current and photocurrent densities of the CsPbBr<sub>3</sub> MC PDs with the PAA at various applied pressures. (H) Power-dependent  $J_{ph}$  and Responsivity at zero bias. (E-H) is quoted with permission from Zhou *et al.*<sup>[105]</sup>. (I) Optical images of FA10 (STP) films. (J) XRD patterns of FA10 (CA) and FA10 (STP) films. (K) On/off ratio of the photodetectors based on FA10 (CA), FA0 (STP), and FA10 (STP) films under different excitation power intensities of 671 nm laser. (L) Light current of FA10 (STP) film photodetectors at 1st and 15th days. (I-L) is quoted with permission from Shang *et al.*<sup>[106]</sup>. (M) Top-view SEM images of the treated films. (N) Influence of the laser power (at 532 nm) on the photostability of the SCTP film photodetector. (O) Linear optical absorption and photoluminescence ( $\lambda_{ex} = 1,030 \text{ nm}$ ) spectra of the CsPbI<sub>1.5</sub>Br<sub>1.5</sub> SCTP film. (P) Photostability of the CA and SCTP film photodetector excited by a 1,030 nm (80 mW power, 15 V bias voltage). (M-P) is quoted with permission from Huang *et al.*<sup>[107]</sup>.

diffusion, and increase the intrinsic resistance of the MAPbI<sub>3</sub> film. The photodetector based on MAPbI<sub>3</sub>/ $\delta$ -FAPbI<sub>3</sub> films exhibited not only superior detection performance but also better stability [Figure 6K and I]. After 15 days of ambient exposure, the photodetector's photocurrent had only decayed by 6%, whereas the MAPbI<sub>3</sub> device treated with STP showed a 16.3% decay [Figure 6L].

In 2022, Huang *et al.* reported a dual-mode perovskite photodetector for both visible and near-infrared light<sup>[107]</sup>, based on a spin-coating thermal-pressed (SCTP) strategy. During the thermal pressing process, an isotropic pressure of 100 MPa was applied to the films, with an elevated annealing temperature of 280 °C due to the fully inorganic nature of the perovskite materials (CsPbI<sub>1.5</sub>Br<sub>1.5</sub>). The SCTP films exhibited excellent crystallinity [Figure 6M] and a substantial improvement in photocurrent, which increased to  $7.16 \times 10^{-5} \text{ A}$  under 532 nm laser irradiation (60 mW), nearly two orders of magnitude higher than that of the control film device ( $1.2 \times 10^{-6} \text{ A}$ ). The dynamic response, shown in Figure 6N, demonstrates that the SCTP film device exhibited enhanced light sensitivity and superior stability. Moreover, the SCTP films also

displayed two-photon absorption characteristics [Figure 6O], generating significant photocurrent in the near-infrared region [Figure 6P], which was not observed in the control films. The study indicates that while the PAC process does not modify the material's structure, it can augment the intrinsic properties of the crystalline material by maximizing its crystallinity. Previously, these physical properties could only be observed at low temperatures.

### X-ray detector

Perovskite-based X-ray detectors typically require a thickness of several hundred micrometers to achieve sufficient X-ray absorption, which cannot be achieved using conventional solution-based spin-coating methods. Additionally, perovskites are highly susceptible to ion migration, a critical issue for detectors operating under high bias. This not only degrades performance but also accelerates material deterioration. The fabrication of perovskite single crystals has been the primary approach to addressing these challenges. However, this method is complex and requires crystal cutting to create devices. An alternative solution involves compressing perovskite microcrystals into wafers through thermal pressing. This method enables the fabrication of wafers with customizable thicknesses and shapes while achieving crystallinity comparable to single crystals.

In 2017, Shrestha *et al.* reported the first X-ray detector based on compressed perovskite wafers<sup>[59]</sup>. Using a hydraulic press, 0.3 GPa of pressure was applied to MAPbI<sub>3</sub> at room temperature for 5 min, producing dense wafers with a 1/2-inch diameter and thicknesses ranging from 200 μm to 1 mm. These wafers exhibited homogeneity and density (3.76 g cm<sup>-3</sup>), closely matching that of single-crystal MAPbI<sub>3</sub> (4.15 g cm<sup>-3</sup>)<sup>[108]</sup>. The wafers also featured a mirror-like reflective surface with a root-mean-square roughness of ~75 nm. However, due to the room-temperature fabrication, the microcrystalline morphology was preserved [Figure 7A]. A self-driven X-ray detector based on these wafers is fabricated, as shown in Figure 7B, with the photocurrent response under constant reverse bias and increasing dose rates presented in Figure 7C. The relationship between the extracted charge and electric field at a constant dose rate of 6.72 mGy<sub>air</sub> s<sup>-1</sup> reveals a high mobility-lifetime product of  $2 \times 10^{-4}$  cm<sup>2</sup> V<sup>-1</sup> [Figure 7D]. Notably, the performance of the detector was comparable to that of a commercial CdTe “Timepix” reference detector. At doses below 5 mGy<sub>air</sub> s<sup>-1</sup>, the extracted charge slightly surpassed that of the CdTe reference, as shown in Figure 7E.

However, pressure treatment at room temperature still fails to effectively promote the fusion and growth of fine grains, leading to devices that exhibit noticeable ion migration [Figure 7C]. This further highlights the importance of heating in the PAC technique.

In 2019, Yang *et al.* employed a combined approach of pressure engineering and annealing to prepare high-quality perovskite wafers<sup>[109]</sup>. They applied a hydraulic pressure of 200 MPa to Cs<sub>2</sub>AgBiBr<sub>6</sub> powders to form the wafer, followed by annealing at 350 °C to enhance the crystallinity of the wafer [Figure 7F]. During this process, BiOBr was introduced to passivate the grain boundaries, thereby inhibiting ion migration, owing to its excellent lattice compatibility with Cs<sub>2</sub>AgBiBr<sub>6</sub>. As shown in Figure 7G, BiOBr-passivated Cs<sub>2</sub>AgBiBr<sub>6</sub> wafers exhibited an ion diffusion barrier of 360 meV, significantly higher than unpassivated wafers (203 meV) and even slightly surpassing single crystals (348 meV). The photocurrent response of Cs<sub>2</sub>AgBiBr<sub>6</sub> wafer-based X-ray detectors under an electric field of 0.1 V μm<sup>-1</sup> is shown in Figure 7H, with a dose rate of 138.7 μGy<sub>air</sub> s<sup>-1</sup>. BiOBr-passivated wafers exhibited a stable baseline and a dark current of ~1 nA, in stark contrast to the increasing dark current of unpassivated wafers. As seen in Figure 7I, detector sensitivity increased linearly from 10 to 250 μC Gy<sub>air</sub><sup>-1</sup> cm<sup>-2</sup> with increasing electric field strength. This sensitivity is 12 times higher than that of α-Se X-ray detectors (20 μC Gy<sub>air</sub><sup>-1</sup> cm<sup>-2</sup>) operating at much higher fields

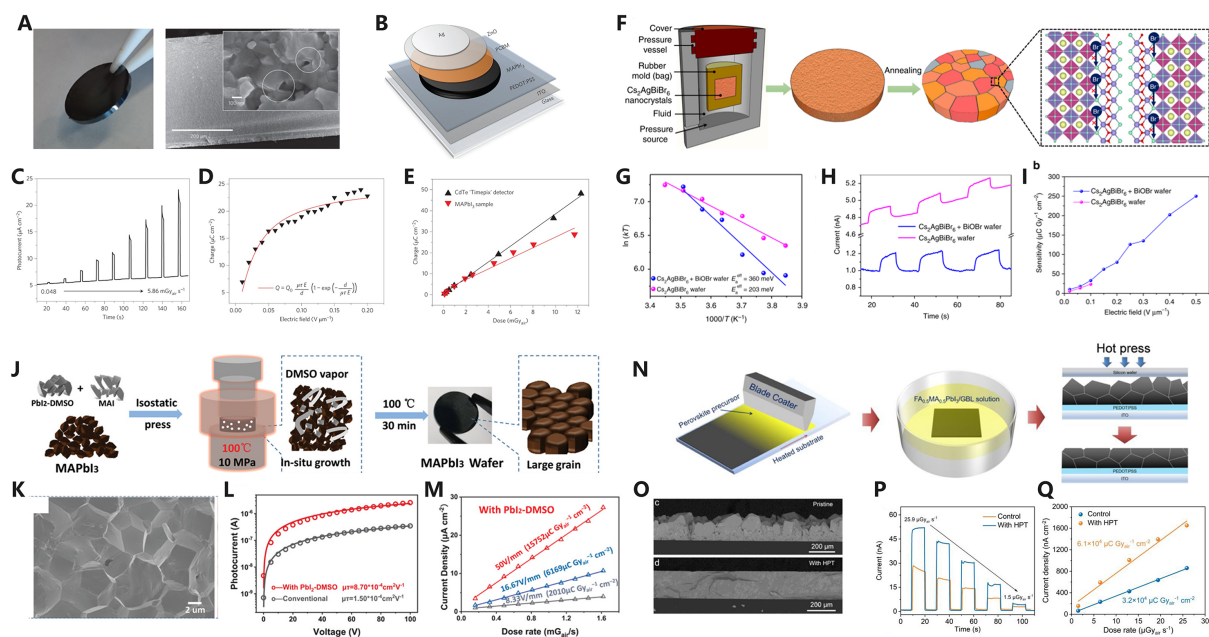


**Figure 7.** (A) The photograph and cross-sectional SEM image of MAPbI<sub>3</sub> wafer. (B) Device stack of the MAPbI<sub>3</sub>-wafer-based X-ray detector. (C) Time-resolved photocurrent at  $E = 0.2 \text{ V } \mu\text{m}^{-1}$  with different dose rates. (D) Extracted charge vs. electric field. (E) Extracted charge for the MAPbI<sub>3</sub> sample and the reference detector. (A-E) is quoted with permission from Shrestha *et al.*<sup>[59]</sup>. (F) Schematic illustration of the isostatic-pressing process. (G) Arrhenius plots of the temperature dependence of  $kT$  vs.  $1,000/T$ . (H) Device response to X-rays ( $138.7 \mu\text{Gy}_{\text{air}} \text{ s}^{-1}$ ) under an electric field of  $0.1 \text{ V } \mu\text{m}^{-1}$ . (I) X-ray sensitivity under different electric fields. (F-I) is quoted with permission from Yang *et al.*<sup>[109]</sup>. (J) Schematic illustration of PbI<sub>2</sub>-DMSO assisted isostatic pressing of the MAPbI<sub>3</sub> wafer. (K) Cross-sectional SEM images, (L) Photoconductivity, and (M) X-ray current densities as a function of the dose rate of PbI<sub>2</sub>-DMSO-assisted MAPbI<sub>3</sub> wafers. (J-M) is quoted with permission from Liu *et al.*<sup>[110]</sup>. (N) Schematic illustration of the preparation process of microcrystalline films. (O) Cross-sectional SEM images, (P) the X-ray response under 0 V bias, and (Q) X-ray photocurrent density vs. dose rate of the pristine and hot-pressed microcrystalline films. (N-Q) is quoted with permission from Li *et al.*<sup>[57]</sup>.

( $10 \text{ V } \mu\text{m}^{-1}$ ). Remarkably, the sensitivity of these polycrystalline wafers surpassed that of Cs<sub>2</sub>AgBiBr<sub>6</sub> single-crystal devices ( $105 \mu\text{C Gy}_{\text{air}}^{-1} \text{ cm}^{-2}$  at  $0.025 \text{ V } \mu\text{m}^{-1}$ ). This study offers a simplified approach to perovskite wafer fabrication without volatile amines, demonstrating the ability to decouple pressing and heating processes. Additionally, the PAC process enables effective doping regardless of dopant solubility, and this method has been proven effective in more research studies<sup>[53]</sup>. In 2022, Liu *et al.* incorporated PbI<sub>2</sub>-DMSO powders into MAPbI<sub>3</sub> wafers to facilitate crystal growth [Figure 7J]<sup>[110]</sup>. The released DMSO vapor facilitates *in situ* growth during the thermocompression treatment process, effectively enhancing crystallinity and reducing defect density. The dense wafers produced featured micron-scale grains [Figure 7K] and exhibited a higher  $\mu\tau$  product compared to wafers without PbI<sub>2</sub>-DMSO additives. X-ray detectors based on these wafers demonstrated a remarkable sensitivity of  $1.58 \times 10^4 \mu\text{C Gy}_{\text{air}}^{-1} \text{ cm}^{-2}$ , as shown in Figure 7L and M.

In 2023, Li *et al.* proposed a method for fabricating dense and smooth perovskite microcrystalline films through polycrystal-induced growth and hot-pressing treatment (HPT)<sup>[57]</sup>. Initially, microcrystalline films were prepared via blade-coating and grown in saturated solutions. The films were then hot-pressed to eliminate voids and smooth their surfaces, as shown in Figure 7N. The resulting films displayed exceptionally flat surfaces and single-crystal-like cross-sectional structures [Figure 7O], with defect levels comparable to those of single crystals<sup>[111,112]</sup>. X-ray detectors fabricated with these films demonstrated significantly higher currents under identical X-ray doses compared to untreated devices, as shown in Figure 7P. By linearly fitting the current density to X-ray dose rates, the HPT-treated devices achieved an impressive sensitivity of  $6.1 \times 10^4 \mu\text{C Gy}_{\text{air}}^{-1} \text{ cm}^{-2}$ , surpassing the  $3.2 \times 10^4 \mu\text{C Gy}_{\text{air}}^{-1} \text{ cm}^{-2}$  sensitivity of control

devices [Figure 7Q]. This work provides an example of large-area fabrication of micron-sized high-quality perovskite films, fully leveraging the advantages of perovskite material preparation. It achieves the production of low-cost, commercially-grade perovskite X-ray detectors, laying a solid foundation for the commercialization of perovskite functional devices.

### Laser

The outstanding luminescent properties of perovskite materials make them an excellent platform for the development of LEDs and lasers<sup>[113]</sup>. In light emission applications, nanotexturing could raise the outcoupling efficiency and impart new features such as directionality and spectral tunability<sup>[114]</sup>. Previous studies have reported optically pumped lasing in single-crystalline perovskite nanowires<sup>[115,116]</sup> and platelets<sup>[117]</sup>, which form naturally high-Q Fabry-Pérot or whispering gallery mode resonators. These studies commonly utilized pre-patterned substrates with resonator structures<sup>[118]</sup>, upon which rough polycrystalline perovskite layers were deposited. The resultant poor crystallinity and surface roughness of the perovskite layers often led to substantial scattering losses and, in certain instances, necessitated cryogenic temperatures to achieve lasing<sup>[119]</sup>. In addition, due to its chemical sensitivity, the conventional wet-chemical lithography technique for photonic nanostructures is not applicable to perovskite materials. Alternatively, nanoimprint lithography, leveraging the soft nature of perovskite materials, not only enables the transfer of patterns onto perovskite films but also enhances the crystalline quality of the films, thereby offering a revolutionary method for creating nanophotonic patterns in perovskite films.

In 2017, Pourdavoud *et al.* were the first to apply nanoimprint lithography (NIL) technology to the patterning of MAPbI<sub>3</sub> films<sup>[120]</sup>. They pressed a shaped stamp onto the MAPbI<sub>3</sub> film at 100 °C with a pressure of 100 bar for 15 min. After imprinting, the perovskite film flawlessly replicated the pattern from the template, forming a regular 2D photonic crystal (2D-PC), and exhibited grain sizes superior to those of the initial film [Figure 8A and B]. Under pump laser excitation, the film displayed narrow spectral emission at 787.6 nm, with an ultra-low lasing threshold of  $E_{\text{thr}} = 3.8 \mu\text{J cm}^{-2}$  [Figure 8C]. The threshold is significantly lower than the  $68.5 \mu\text{J cm}^{-2}$  reported for perovskite layers deposited on pre-patterned 2D-PC substrates. Additionally, the laser emission wavelength can be tuned between 778.8 and 800.8 nm by adjusting the film thickness, as shown in Figure 8D, which influences the effective refractive index. One year later, they developed distributed feedback (DFB) lasers based on MAPbBr<sub>3</sub> [Figure 8E]<sup>[121]</sup>. They used the NIL process to fabricate linear gratings with a 300 nm period on MAPbBr<sub>3</sub> thin films [Figure 8F]. The spectral emission characteristics of the MAPbBr<sub>3</sub> DFB laser under increasing optical excitation densities, ranging from 0.5 to  $5 \mu\text{J cm}^{-2}$ , are shown in Figure 8G. When the excitation power exceeded  $3.4 \mu\text{J cm}^{-2}$ , the laser emitted at 555.3 nm with a linewidth of  $\Delta\lambda = 0.14 \text{ nm}$  [Figure 8H]. These groundbreaking studies on achieving low-threshold lasing in perovskite materials demonstrate tremendous potential, significantly expanding the functional applications of perovskites, particularly highlighting the versatility of PAC technology in precisely regulating the multidimensional properties of perovskite materials. However, current research on patterned perovskite lasers remains in its preliminary stages, primarily focusing on the use of imprinting techniques to construct perovskite photonic crystal structures, while the changes in the luminescent properties of perovskite materials after the PAC process have not been thoroughly explored. Additionally, a systematic theoretical model linking patterned morphology, material defect levels, and device luminescent performance has yet to be established, necessitating further in-depth research.

### SUMMARY AND OUTLOOK

The PAC technique complements the development of perovskite materials by fully utilizing the soft lattice characteristics of perovskite materials and cleverly combining the thermal processing properties of polycrystalline perovskites. This approach has successfully achieved the transformation of perovskite

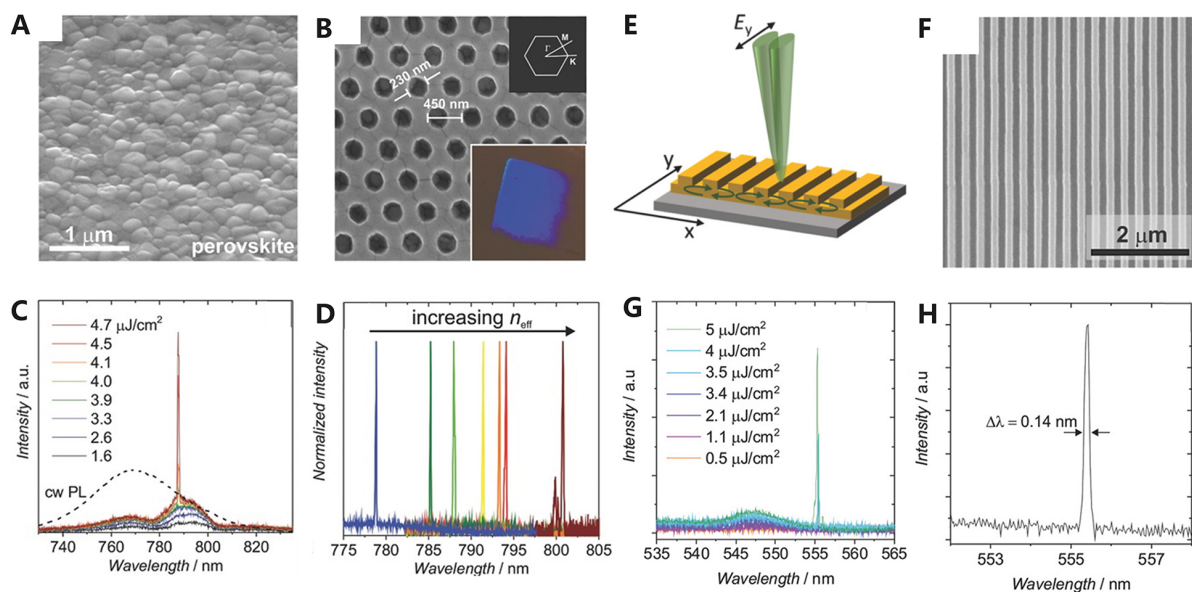


**Figure 8.** Top-view SEM image of (A) the pristine MAPbBr<sub>3</sub> perovskite layer and (B) the 2D-PC. (C) Emission spectra upon optical pumping with increasing energy density 1.6–4.7 μJ cm<sup>-2</sup>. (D) Tunability of the laser emission upon variation of the excitation spot on the sample. (A–D) is quoted with permission from Pourdavoud *et al.*<sup>[120]</sup>. (E) Schematic of the DFB laser with the assignment of directions and a sketch of the laser emission as a result of first-order diffraction normal to the sample surface. (F) SEM images of the DFB grating imprinted into the MAPbBr<sub>3</sub> layer. (G) Emission spectra upon optical pumping with increasing energy density 0.5–5 μJ cm<sup>-2</sup>. (H) Emission spectrum of the laser measured with high spectral resolution. (E–H) is quoted with permission from Pourdavoud *et al.*<sup>[121]</sup>.

materials from initial fine grains to quasi-single crystals. This transformation process is markedly different from traditional research paths in the field of pressure engineering, which focus on high-pressure-induced crystal phase transitions and crystal growth under high-pressure conditions. This paper systematically reviews the recent research progress of the PAC technique in the preparation of perovskite materials, covering its effects and device applications, and providing a comprehensive outline of the development trajectory of this technique. A detailed exploration of its mechanisms is also included. Numerous studies have shown that low-pressure-assisted crystallization significantly improves the crystallization quality of perovskite thin films and wafers, greatly reducing their defect density. Additionally, this technique offers unique advantages, such as the elimination of voids and optimization of crystal orientation. It is currently the leading process for producing polycrystalline perovskites with crystallinity approaching that of single crystals, while also offering the flexibility and cost-effectiveness that single-crystal perovskites cannot. Today, the PAC technique has achieved remarkable results, amplifying the inherent advantages of perovskite materials and overcoming the limitations of traditional processing techniques. However, as a relatively recent development alongside perovskite material research, the PAC technique still faces many challenges. We remain hopeful for the future development of this technique and look forward to its continuous breakthroughs, offering new ideas and solutions to address existing problems.

#### (i) Imperfect pressure action mechanism

Despite numerous studies on the functional applications of the PAC process, a comprehensive understanding of the underlying mechanisms remains lacking. There is still considerable debate regarding the exact role of pressure during the recrystallization process and the grain growth behavior. In addition, current monitoring methods are insufficient, lacking high-precision, *in situ* characterization techniques to observe crystal growth during PAC, which limits the development of accurate crystal growth models.

(ii) Imprecise processing parameters

The absence of a thorough understanding of key perovskite material parameters (e.g., activation energy, grain boundary mobility) results in a lack of precision in selecting processing temperatures and pressures. To improve the controllability and efficiency of PAC processes, further systematic research is needed to determine and standardize the optimal processing conditions for the PAC process.

(iii) Lack of performance-leading functional devices

While the PAC technique has enabled the transformation of fine grains into quasi-single crystals, leading to significant improvements in the performance of functional devices, some devices based on these films have yet to achieve performance superiority. This is particularly evident in vertical-structure devices with complex layer configurations, where performance, though commendable, still falls significantly short of the leading-edge levels achieved by single-crystal or quasi-single-crystal devices. For instance, while advanced perovskite solar cells have achieved certified efficiencies exceeding 26%, devices fabricated using the PAC process have not yet surpassed 25% efficiency. This performance gap highlights the suboptimal nature of current PAC technology, which may be attributed to mechanical peeling and chemical degradation issues arising from interactions between the pressure plate and the film interface. A critical challenge for future research lies in effectively eliminating surface damage during the PAC process to overcome the current performance bottleneck. Promising solutions are emerging: the rapidly developing self-assembled monolayer (SAM) technology offers a potential pathway to reduce interface damage, while chemical repair methods, such as methylamine gas treatment<sup>[122,123]</sup>, have been proven to significantly enhance the interface quality of perovskite films. Integrating these two technologies into the PAC process holds great promise for addressing the existing limitations. By further optimizing the PAC technique and improving the performance of large-grain perovskite film devices, a broader question can also be explored: whether single-crystal or quasi-single-crystal perovskite films are essential for commercial applications, particularly when balancing manufacturing costs and commercial benefits. This optimization could pave the way for more cost-effective and scalable production of high-performance perovskite devices.

(iv) Limited expansion to other materials

The PAC technique is mainly applied to perovskite materials. However, many other materials with similar properties, such as PbS, which also exhibits a soft lattice structure, could benefit from this technique. Expanding its application to these materials will help refine the underlying mechanisms, validate its effectiveness, and accelerate the development and maturation of the technique. This, in turn, will contribute to the further advancement of perovskite-based functional devices.

## DECLARATIONS

### Acknowledgments

Special thanks to XingQi Ji, Rui Li, and Xiangyu Li for the support they provided during the preparation of this article.

### Authors' contributions

Made the literature review and drafted the original version: Yu, Y.

Revised the manuscript: Du, H.; Liu, Q.

Conceived and supervised the project: Pang, Z.

### Availability of data and materials

Not applicable.

### Financial support and sponsorship

This research work was supported by the National Natural Science Foundation of China (No. 12274259) and the Shandong Province Natural Science Foundation (ZR2023LZH002 and ZR2024QA164).

### Conflicts of interest

All authors declared that there are no conflicts of interest.

### Ethical approval and consent to participate

Not applicable.

### Consent for publication

Not applicable.

### Copyright

© The Author(s) 2025.

## REFERENCES

1. Kojima, A.; Teshima, K.; Shirai, Y.; Miyasaka, T. Organometal halide perovskites as visible-light sensitizers for photovoltaic cells. *J. Am. Chem. Soc.* **2009**, *131*, 6050-1. [DOI](#)
2. Zhang, P.; Wu, J.; Zhang, T.; et al. Perovskite solar cells with ZnO electron-transporting materials. *Adv. Mater.* **2018**, *30*, 1703737. [DOI](#)
3. Liu, D.; Kelly, T. L. Perovskite solar cells with a planar heterojunction structure prepared using room-temperature solution processing techniques. *Nat. Photon.* **2014**, *8*, 133-8. [DOI](#)
4. Das, S.; Yang, B.; Gu, G.; et al. High-performance flexible perovskite solar cells by using a combination of ultrasonic spray-coating and low thermal budget photonic curing. *ACS. Photonics.* **2015**, *2*, 680-6. [DOI](#)
5. Ma, C.; Zhang, C.; Chen, S.; et al. Interfacial defect passivation by multiple-effect molecule for efficient and stable perovskite solar cells. *Solar. Energy. Mater. Solar. Cells.* **2023**, *262*, 112499. [DOI](#)
6. Zheng, X.; Li, Z.; Zhang, Y.; et al. Co-deposition of hole-selective contact and absorber for improving the processability of perovskite solar cells. *Nat. Energy.* **2023**, *8*, 462-72. [DOI](#)
7. Kim, J. Y.; Lee, J. W.; Jung, H. S.; Shin, H.; Park, N. G. High-efficiency perovskite solar cells. *Chem. Rev.* **2020**, *120*, 7867-918. [DOI](#)
8. Qu, M.; Tian, Y.; Cheng, Y.; Zhong, J.; Zhang, C. Whole-device mass-producible perovskite photodetector based on laser-induced graphene electrodes. *Adv. Opt. Mater.* **2022**, *10*, 2201741. [DOI](#)
9. Zhan, Y.; Cheng, Q.; Peng, J.; et al. Nacre inspired robust self-encapsulating flexible perovskite photodetector. *Nano. Energy.* **2022**, *98*, 107254. [DOI](#)
10. Zhu, B. S.; Ma, Z. Y.; Song, Y. H.; et al. Ultrabright and efficient green perovskite light-emitting diodes enabled by well-crystallized dense CsPbBr<sub>3</sub> nanocubes. *Nano. Lett.* **2024**, *24*, 14750-7. [DOI](#)
11. Liu, L.; Xu, M.; Xu, X.; Tao, X.; Gao, Z. High sensitivity X-ray detectors with low degradation based on deuterated halide perovskite single crystals. *Adv. Mater.* **2024**, *36*, e2406443. [DOI](#)
12. Wei, H.; Gong, J.; Liu, J.; et al. Thermally and mechanically stable perovskite artificial synapse as tuned by phase engineering for efferent neuromuscular control. *Nano. Lett.* **2024**, *24*, 9311-21. [DOI](#)
13. Wang, J.; Zhang, C.; Liu, H.; et al. Tunable spin characteristic properties in spin valve devices based on hybrid organic-inorganic perovskites. *Adv. Mater.* **2019**, *31*, e1904059. [DOI](#)
14. Ashley, M. J.; O'Brien, M. N.; Hedderick, K. R.; Mason, J. A.; Ross, M. B.; Mirkin, C. A. Templated synthesis of uniform perovskite nanowire arrays. *J. Am. Chem. Soc.* **2016**, *138*, 10096-9. [DOI](#) [PubMed](#)
15. Tang, S.; Deng, Y.; Zheng, X.; et al. Composition engineering in doctor-blading of perovskite solar cells. *Adv. Energy. Mater.* **2017**, *7*, 1700302. [DOI](#)
16. Zhang, Y.; Liu, Y.; Liu, S. Composition engineering of perovskite single crystals for high-performance optoelectronics. *Adv. Funct. Mater.* **2023**, *33*, 2210335. [DOI](#)
17. Yu, J. C.; Li, B.; Dunn, C. J.; et al. High-performance and stable semi-transparent perovskite solar cells through composition engineering. *Adv. Sci.* **2022**, *9*, e2201487. [DOI](#)
18. Li, Q.; Wang, Y.; Pan, W.; et al. High-pressure band-gap engineering in lead-free Cs<sub>2</sub>AgBiBr<sub>6</sub> double perovskite. *Angew. Chem. Int.*

- Ed.* 2017, 56, 15969-73. DOI
19. Ren, X.; Yan, X.; Ahmad, A. S.; et al. Pressure-induced phase transition and band gap engineering in propylammonium lead bromide perovskite. *J. Phys. Chem. C* 2019, 123, 15204-8. DOI
  20. Francisco-López, A.; Charles, B.; Weber, O. J.; et al. Pressure-induced locking of methylammonium cations versus amorphization in hybrid lead iodide perovskites. *J. Phys. Chem. C* 2018, 122, 22073-82. DOI
  21. Wang, Y.; Lü, X.; Yang, W.; et al. Pressure-induced phase transformation, reversible amorphization, and anomalous visible light response in organolead bromide perovskite. *J. Am. Chem. Soc.* 2015, 137, 11144-9. DOI
  22. Yuan, Y.; Liu, X. F.; Ma, X.; et al. Large band gap narrowing and prolonged carrier lifetime of (C<sub>4</sub>H<sub>9</sub>NH<sub>3</sub>)<sub>2</sub>PbI<sub>4</sub> under high pressure. *Adv. Sci.* 2019, 6, 1900240. DOI PubMed PMC
  23. Wang, Y.; Long, R. Unravelling the effects of pressure-induced suppressed electron-hole recombination in CsPbBr<sub>3</sub> perovskite: time-domain ab initio analysis. *J. Phys. Chem. Lett.* 2019, 10, 4354-61. DOI
  24. Sarkar, G.; Ghosh, D. Effects of lattice compression on halogen ion diffusion dynamics in mixed halide perovskites. *ACS. Appl. Energy. Mater.* 2024, 7, 6376-83. DOI
  25. Vishnoi, P.; Rao, C. N. R. Temperature and pressure induced structural transitions of lead iodide perovskites. *J. Mater. Chem. A* 2023, 12, 19-37. DOI
  26. Capitani, F.; Marini, C.; Caramazza, S.; et al. High-pressure behavior of methylammonium lead iodide (MAPbI<sub>3</sub>) hybrid perovskite. *J. Appl. Phys.* 2016, 119, 185901. DOI
  27. Morozova, N. V.; Zhevstovskikh, I. V.; Korobeinikov, I. V.; Sarychev, M. N.; Semenova, O. I.; Ovsyannikov, S. V. Manipulating the phase stability of a halide perovskite, CH<sub>3</sub>NH<sub>3</sub>PbI<sub>3</sub> by high-pressure cycling. *J. Alloys. Compd.* 2024, 988, 174305. DOI
  28. Wang, H.; Wang, Q.; Yang, K.; et al. The self-healing and robust photostability of (PEA)<sub>2</sub>PbI<sub>4</sub> perovskite via pressure-induced amorphization and recrystallization. *Opt. Mater.* 2024, 152, 115449. DOI
  29. Nie, W.; Tsai, H.; Blancon, J. C.; et al. Critical role of interface and crystallinity on the performance and photostability of perovskite solar cell on nickel oxide. *Adv. Mater.* 2018, 30, 1703879. DOI
  30. Shao, S.; Dong, J.; Duim, H.; et al. Enhancing the crystallinity and perfecting the orientation of formamidinium tin iodide for highly efficient Sn-based perovskite solar cells. *Nano. Energy.* 2019, 60, 810-6. DOI
  31. Ahmadian-yazdi, M.; Lin, S.; Cai, Z. Unveiling heavy heterovalent doping-modulated microstructure and thermoelectric performance in bulk hybrid perovskite single crystals. *Chem. Eng. J.* 2024, 487, 150477. DOI
  32. Zhou, B.; Ding, D.; Wang, Y.; et al. A scalable H<sub>2</sub>O-DMF-DMSO solvent synthesis of highly luminescent inorganic perovskite-related cesium lead bromides. *Adv. Opt. Mater.* 2021, 9, 2001435. DOI
  33. Manjunatha, S. N.; Chu, Y.; Jeng, M.; Chang, L. The Characteristics of perovskite solar cells fabricated using DMF and DMSO/GBL solvents. *J. Electron. Mater.* 2020, 49, 6823-8. DOI
  34. Zhang, F.; Lian, J.; Song, J.; Hao, Y.; Zeng, P.; Niu, H. Sec-butyl alcohol assisted pinhole-free perovskite film growth for high-performance solar cells. *J. Mater. Chem. A* 2016, 4, 3438-45. DOI
  35. Xiao, M.; Huang, F.; Huang, W.; et al. A fast deposition-crystallization procedure for highly efficient lead iodide perovskite thin-film solar cells. *Angew. Chem. Int. Ed.* 2014, 53, 9898-903. DOI
  36. Chen, J.; Ren, J.; Li, Z.; Wang, H.; Hao, Y. Mixed antisolvents assisted treatment of perovskite for photovoltaic device efficiency enhancement. *Org. Electron.* 2018, 56, 59-67. DOI
  37. Li, X.; Dar, M. I.; Yi, C.; et al. Improved performance and stability of perovskite solar cells by crystal crosslinking with alkylphosphonic acid ω-ammonium chlorides. *Nat. Chem.* 2015, 7, 703-11. DOI
  38. Wu, Z.; Raga, S. R.; Juarez-Perez, E. J.; et al. Improved efficiency and stability of perovskite solar cells induced by C=O functionalized hydrophobic ammonium-based additives. *Adv. Mater.* 2018, 30, 1703670. DOI
  39. Ahn, N.; Son, D. Y.; Jang, I. H.; Kang, S. M.; Choi, M.; Park, N. G. Highly reproducible perovskite solar cells with average efficiency of 18.3% and best efficiency of 19.7% fabricated via lewis base adduct of lead(II) iodide. *J. Am. Chem. Soc.* 2015, 137, 8696-9. DOI PubMed
  40. Noel, N. K.; Abate, A.; Stranks, S. D.; et al. Enhanced photoluminescence and solar cell performance via Lewis base passivation of organic-inorganic lead halide perovskites. *ACS. Nano.* 2014, 8, 9815-21. DOI
  41. Xiao, Z.; Dong, Q.; Bi, C.; Shao, Y.; Yuan, Y.; Huang, J. Solvent annealing of perovskite-induced crystal growth for photovoltaic-device efficiency enhancement. *Adv. Mater.* 2014, 26, 6503-9. DOI
  42. Xie, F. X.; Zhang, D.; Su, H.; et al. Vacuum-assisted thermal annealing of CH<sub>3</sub>NH<sub>3</sub>PbI<sub>3</sub> for highly stable and efficient perovskite solar cells. *ACS. Nano.* 2015, 9, 639-46. DOI
  43. Liu, J.; Gao, C.; He, X.; et al. Improved crystallization of perovskite films by optimized solvent annealing for high efficiency solar cell. *ACS. Appl. Mater. Interfaces.* 2015, 7, 24008-15. DOI
  44. Gao, L.; Li, C.; Li, C.; Yang, G. Large-area high-efficiency perovskite solar cells based on perovskite films dried by the multi-flow air knife method in air. *J. Mater. Chem. A* 2017, 5, 1548-57. DOI
  45. Zhong, J.; Wu, W.; Ding, L.; Kuang, D. Blade-coating perovskite films with diverse compositions for efficient photovoltaics. *Energy. Environ. Mater.* 2021, 4, 277-83. DOI
  46. Li, Z.; Wang, X.; Wang, Z.; et al. Ammonia for post-healing of formamidinium-based Perovskite films. *Nat. Commun.* 2022, 13, 4417. DOI PubMed PMC
  47. Su, J.; Cai, H.; Ye, X.; et al. Efficient Perovskite solar cells prepared by hot air blowing to ultrasonic spraying in ambient air. *ACS.*

- Appl. Mater. Interfaces*. 2019, 11, 10689-96. DOI
48. Zhang, Z.; Li, Z.; Deng, L.; et al. Hot-air treatment-regulated diffusion of LiTFSI to accelerate the aging-induced efficiency rising of perovskite solar cells. *ACS Appl. Mater. Interfaces*. 2022, 14, 4378-88. DOI
49. Meng, K.; Chen, B.; Xiao, M.; et al. Humidity-insensitive, large-area-applicable, hot-air-assisted ambient fabrication of 2D perovskite solar cells. *Adv. Mater.* 2023, 35, e2209712. DOI
50. Xing, R.; Shi, P.; Wang, D.; et al. Flexible self-powered weak light detectors based on ZnO/CsPbBr<sub>3</sub>/γ-CuI heterojunctions. *ACS Appl. Mater. Interfaces*. 2022, 14, 40093-101. DOI
51. Zhu, F.; Lian, G.; Cui, D.; et al. A general strategy for ordered carrier transport of quasi-2D and 3D Perovskite films for giant self-powered photoresponse and ultrahigh stability. *Nanomicro. Lett.* 2023, 15, 115. DOI PubMed PMC
52. Witt, C.; Leupold, N.; Ramming, P.; Schötz, K.; Moos, R.; Panzer, F. How the microstructure of MAPbI<sub>3</sub> powder impacts pressure-induced compaction and optoelectronic thick-film properties. *J. Phys. Chem. C*. 2022, 126, 15424-35. DOI
53. Liu, L.; Li, W.; Feng, X.; et al. Energy transfer assisted fast X-ray detection in direct/indirect hybrid perovskite wafer. *Adv. Sci.* 2022, 9, e2103735. DOI PubMed PMC
54. Shi, Y.; Zhou, Y.; Ma, Z.; Xiao, G.; Wang, K.; Zou, B. Structural regulation and optical behavior of three-dimensional metal halide perovskites under pressure. *J. Mater. Chem. C*. 2020, 8, 12755-67. DOI
55. Liu, G.; Kong, L.; Yang, W.; Mao, H. Pressure engineering of photovoltaic perovskites. *Mater. Today*. 2019, 27, 91-106. DOI
56. Wang, N.; Zhang, S.; Wang, S.; et al. Pressure engineering on perovskite structures, properties, and devices. *Adv. Funct. Mater.* 2024, 34, 2315918. DOI
57. Li, N.; Li, Y.; Xie, S.; et al. High-performance and self-powered X-ray detectors made of smooth perovskite microcrystalline films with 100 μm grains. *Angew. Chem. Int. Ed.* 2023, 62, e202302435. DOI
58. Liu, Y.; Wu, Z.; Dou, Y.; et al. Formamidinium-based perovskite solar cells with enhanced moisture stability and performance via confined pressure annealing. *J. Phys. Chem. C*. 2020, 124, 12249-58. DOI
59. Shrestha, S.; Fischer, R.; Matt, G. J.; et al. High-performance direct conversion X-ray detectors based on sintered hybrid lead triiodide perovskite wafers. *Nat. Photon.* 2017, 11, 436-40. DOI
60. Li, W. G.; Wang, X. D.; Huang, Y. H.; Kuang, D. B. Ultrasound-assisted crystallization enables large-area perovskite quasi-monocrystalline film for high-sensitive X-ray detection and imaging. *Adv. Mater.* 2023, 35, e2210878. DOI PubMed
61. Zhang, H. J.; Liu, Y. F.; Zheng, X.; Feng, J. Improved performance of all-inorganic perovskite light-emitting diodes via nanostructured stamp imprinting. *Chemphyschem* 2023, 24, e202200860. DOI
62. Mosconi, E.; De, A. F. Mobile ions in organohalide perovskites: interplay of electronic structure and dynamics. *ACS. Energy. Lett.* 2016, 1, 182-8. DOI
63. Yang, R. X.; Skelton, J. M.; da, S. E. L.; Frost, J. M.; Walsh, A. Spontaneous octahedral tilting in the cubic inorganic cesium halide perovskites CsSnX<sub>3</sub> and CsPbX<sub>3</sub> (X = F, Cl, Br, I). *J. Phys. Chem. Lett.* 2017, 8, 4720-6. DOI
64. Fabini, D. H.; Seshadri, R.; Kanatzidis, M. G. The underappreciated lone pair in halide perovskites underpins their unusual properties. *MRS. Bull.* 2020, 45, 467-77. DOI
65. Reyes-Martinez, M. A.; Abdelhady, A. L.; Saidaminov, M. I.; et al. Time-dependent mechanical response of APbX<sub>3</sub> (A = Cs, CH<sub>3</sub>NH<sub>3</sub>; X = I, Br) single crystals. *Adv. Mater.* 2017, 29, 1606556. DOI
66. Rakita, Y.; Cohen, S. R.; Kedem, N. K.; Hodes, G.; Cahen, D. Mechanical properties of APbX<sub>3</sub> (A = Cs or CH<sub>3</sub>NH<sub>3</sub>; X = I or Br) perovskite single crystals. *MRS. Commun.* 2015, 5, 623-9. DOI
67. Li, M.; Li, H.; Li, W.; et al. Oriented 2D Perovskite wafers for anisotropic X-ray detection through a fast tableting strategy. *Adv. Mater.* 2022, 34, e2108020. DOI
68. Witt, C.; Schmid, A.; Leupold, N.; et al. Impact of pressure and temperature on the compaction dynamics and layer properties of powder-pressed methylammonium lead halide thick films. *ACS Appl. Electron. Mater.* 2020, 2, 2619-28. DOI
69. Matsushima, T.; Fujihara, T.; Qin, C.; et al. Morphological control of organic-inorganic perovskite layers by hot isostatic pressing for efficient planar solar cells. *J. Mater. Chem. A*. 2015, 3, 17780-7. DOI
70. Mayer, A.; Haeger, T.; Runkel, M.; et al. Relevance of processing parameters for grain growth of metal halide perovskites with nanoimprint. *Appl. Phys. A*. 2021, 127, 4830. DOI
71. Dunlap-shohl, W. A.; Li, T.; Mitzi, D. B. Interfacial effects during rapid lamination within MAPbI<sub>3</sub> thin films and solar cells. *ACS Appl. Energy. Mater.* 2019, 2, 5083-93. DOI
72. Mayer, A.; Pourdavoud, N.; Doukkali, Z.; et al. Upgrading of methylammonium lead halide perovskite layers by thermal imprint. *Appl. Phys. A*. 2021, 127, 4366. DOI
73. Moon, J.; Kwon, S.; Alahbakhshi, M.; et al. Surface energy-driven preferential grain growth of metal halide perovskites: effects of nanoimprint lithography beyond direct patterning. *ACS Appl. Mater. Interfaces*. 2021, 13, 5368-78. DOI
74. Palmer, J. E.; Thompson, C. V.; Smith, H. I. Grain growth and grain size distributions in thin germanium films. *J. Appl. Phys.* 1987, 62, 2492-7. DOI
75. Thompson, C. V. Grain growth in thin films. *Annu. Rev. Mater. Sci.* 1990, 20, 245-68. DOI
76. Thompson, C. V. Structure evolution during processing of polycrystalline films. *Annu. Rev. Mater. Sci.* 2000, 30, 159-90. DOI
77. Mayer, A.; Haeger, T.; Runkel, M.; et al. Direct patterning of methylammonium lead bromide perovskites by thermal imprint. *Appl. Phys. A*. 2022, 128, 5521. DOI
78. Fu, X.; Dong, N.; Lian, G.; et al. High-quality CH<sub>3</sub>NH<sub>3</sub>PbI<sub>3</sub> films obtained via a pressure-assisted space-confined solvent-engineering

- strategy for ultrasensitive photodetectors. *Nano. Lett.* **2018**, *18*, 1213-20. DOI
79. Thompson, C.; Carel, R. Texture development in polycrystalline thin films. *Mater. Sci. Eng. B.* **1995**, *32*, 211-9. DOI
80. Thompson, C. Grain growth in polycrystalline thin films of semiconductors. *Interface. Sci.* **1998**, *6*, 85-93. DOI
81. Wang, T.; Lian, G.; Huang, L.; et al. MAPbI<sub>3</sub> quasi-single-crystal films composed of large-sized grains with deep boundary fusion for sensitive vis-NIR photodetectors. *ACS. Appl. Mater. Interfaces.* **2020**, *12*, 38314-24. DOI
82. Zhang, L.; Zhang, T.; Gao, Y.; et al. Uniaxially oriented FA<sub>x</sub>MA<sub>1-x</sub>PbI<sub>3</sub> films with low intragrain and structural defects for self-powered photodetectors. *J. Mater. Chem. C.* **2022**, *10*, 9546-53. DOI
83. Zheng, L.; Nozariasbmarz, A.; Hou, Y.; et al. A universal all-solid synthesis for high throughput production of halide perovskite. *Nat. Commun.* **2022**, *13*, 7399. DOI PubMed PMC
84. Zhang, H.; Hou, W.; Hao, Y.; Song, J.; Zhang, F. Unified crystal phase control with MACl for inducing single-crystal-like perovskite thin films in high-pressure fusion toward high efficiency perovskite solar cell modules. *Small* **2024**, *20*, e2400173. DOI
85. Zhang, J.; Liu, F.; Li, S.; et al. Recrystallization behaviour of cubic boron nitride under high pressure. *J. Eur. Ceram. Soc.* **2021**, *41*, 132-8. DOI
86. Yin, T.; Fang, Y.; Chong, W. K.; et al. High-pressure-induced comminution and recrystallization of CH<sub>3</sub>NH<sub>3</sub>PbBr<sub>3</sub> nanocrystals as large thin nanoplates. *Adv. Mater.* **2018**, *30*, 1705017. DOI
87. Lee, K. J.; Wei, R.; Wang, Y.; et al. Gigantic suppression of recombination rate in 3D lead-halide perovskites for enhanced photodetector performance. *Nat. Photon.* **2023**, *17*, 236-43. DOI
88. Shao, Y.; Fang, Y.; Li, T.; et al. Grain boundary dominated ion migration in polycrystalline organic-inorganic halide perovskite films. *Energy. Environ. Sci.* **2016**, *9*, 1752-9. DOI
89. Sherkar, T. S.; Momblona, C.; Gil-Escrig, L.; et al. Recombination in perovskite solar cells: significance of grain boundaries, interface traps, and defect ions. *ACS. Energy. Lett.* **2017**, *2*, 1214-22. DOI PubMed PMC
90. Luo, J.; Xia, J.; Yang, H.; et al. A pressure process for efficient and stable perovskite solar cells. *Nano. Energy.* **2020**, *77*, 105063. DOI
91. Chun, D. H.; Kim, S.; Chai, S. U.; et al. Grain boundary healing of organic-inorganic halide perovskites for moisture stability. *Nano. Lett.* **2019**, *19*, 6498-505. DOI
92. Lanaghan, C. L.; Okia, O.; Coons, T.; et al. Understanding process-structure relationships during lamination of halide perovskite interfaces. *ACS. Appl. Mater. Interfaces.* **2024**, *16*, 58657-67. DOI
93. Yang, B.; Xie, Y.; Zeng, P.; Dong, Y.; Ou, Q.; Zhang, S. Tightly compacted perovskite laminates on flexible substrates via hot-pressing. *Appl. Sci.* **2020**, *10*, 1917. DOI
94. Zhang, W.; Li, Y.; Liu, X.; Tang, D.; Li, X.; Yuan, X. Ethyl acetate green antisolvent process for high-performance planar low-temperature SnO<sub>2</sub>-based perovskite solar cells made in ambient air. *Chem. Eng. J.* **2020**, *379*, 122298. DOI
95. Wang, T.; Lian, G.; Huang, L.; et al. A crystal-growth boundary-fusion strategy to prepare high-quality MAPbI<sub>3</sub> films for excellent Vis-NIR photodetectors. *Nano. Energy.* **2019**, *64*, 103914. DOI
96. Huang, L.; Xing, Z.; Tang, X.; et al. Toward efficient perovskite solar cells by planar imprint for improved perovskite film quality and granted bifunctional barrier. *J. Mater. Chem. A.* **2021**, *9*, 16178-86. DOI
97. Chen, H.; Ye, F.; Tang, W.; et al. A solvent- and vacuum-free route to large-area perovskite films for efficient solar modules. *Nature* **2017**, *550*, 92-5. DOI
98. Yu, Y.; Shang, M.; Wang, T.; et al. All-round performance improvement of semitransparent perovskite solar cells by a pressure-assisted method. *J. Mater. Chem. C.* **2021**, *9*, 15056-64. DOI
99. Zhang, H.; Ye, S.; Hao, Y.; et al. Realization of ultra-flat perovskite films with surprisingly large-grain distribution using high-pressure cooking. *Chem. Eng. J.* **2022**, *445*, 136803. DOI
100. Zhu, F.; Lian, G.; Yu, B.; et al. Pressure-enhanced vertical orientation and compositional control of ruddlesden-popper perovskites for efficient and stable solar cells and self-powered photodetectors. *ACS. Appl. Mater. Interfaces.* **2022**, *14*, 1526-36. DOI
101. Li, T.; Dunlap-shohl, W. A.; Mitzi, D. B. Bifacial perovskite solar cells via a rapid lamination process. *ACS. Appl. Energy. Mater.* **2020**, *3*, 9493-7. DOI
102. Gan, S.; Sun, H.; Li, C.; Dou, D.; Li, L. Bifacial perovskite solar cells: a universal component that goes beyond albedo utilization. *Sci. Bull.* **2023**, *68*, 2247-67. DOI
103. Yadavalli, S. K.; Lanaghan, C. L.; Palmer, J.; et al. Lamination of >21% efficient perovskite solar cells with independent process control of transport layers and interfaces. *ACS. Appl. Mater. Interfaces.* **2024**, *16*, 16040-9. DOI
104. Dong, N.; Fu, X.; Lian, G.; et al. Solvent-assisted thermal-pressure strategy for constructing high-quality CH<sub>3</sub>NH<sub>3</sub>PbI<sub>3-x</sub>Cl<sub>x</sub> films as high-performance perovskite photodetectors. *ACS. Appl. Mater. Interfaces.* **2018**, *10*, 8393-8. DOI
105. Zhou, H.; Song, Z.; Grice, C. R.; et al. Pressure-assisted annealing strategy for high-performance self-powered all-inorganic perovskite microcrystal photodetectors. *J. Phys. Chem. Lett.* **2018**, *9*, 4714-9. DOI
106. Shang, M.; Lian, G.; Lv, S.; et al. "Visible" phase separation of MAPbI<sub>3</sub>/δ-FAPbI<sub>3</sub> films for high-performance and stable photodetectors. *Adv. Mater. Inter.* **2021**, *8*, 2100266. DOI
107. Huang, L.; Yu, B.; Zhu, F.; et al. Spin-coating thermal-pressed strategy for the preparation of inorganic perovskite quasi-single-crystal thin films with giant single-/two-photon responses. *Nano. Energy.* **2022**, *92*, 106719. DOI
108. Stoumpos, C. C.; Malliakas, C. D.; Kanatzidis, M. G. Semiconducting tin and lead iodide perovskites with organic cations: phase transitions, high mobilities, and near-infrared photoluminescent properties. *Inorg. Chem.* **2013**, *52*, 9019-38. DOI PubMed

109. Yang, B.; Pan, W.; Wu, H.; et al. Heteroepitaxial passivation of Cs<sub>2</sub>AgBiBr<sub>6</sub> wafers with suppressed ionic migration for X-ray imaging. *Nat. Commun.* **2019**, *10*, 1989. [DOI](#) [PubMed](#) [PMC](#)
110. Liu, W.; Shi, T.; Zhu, J.; et al. PbI<sub>2</sub>-DMSO assisted in situ growth of perovskite wafers for sensitive direct X-ray detection. *Adv. Sci.* **2022**, *10*, e2204512. [DOI](#) [PubMed](#) [PMC](#)
111. Wu, J.; Wang, L.; Feng, A.; et al. Self-powered FA<sub>0.55</sub>MA<sub>0.45</sub>PbI<sub>3</sub> single-crystal perovskite X-ray detectors with high sensitivity. *Adv. Funct. Mater.* **2022**, *32*, 2109149. [DOI](#)
112. Wang, W.; Meng, H.; Qi, H.; et al. Electronic-grade high-quality perovskite single crystals by a steady self-supply solution growth for high-performance X-ray detectors. *Adv. Mater.* **2020**, *32*, e2001540. [DOI](#)
113. Stranks, S. D.; Snaith, H. J. Metal-halide perovskites for photovoltaic and light-emitting devices. *Nat. Nanotechnol.* **2015**, *10*, 391-402. [DOI](#) [PubMed](#)
114. Zhmakin, A. Enhancement of light extraction from light emitting diodes. *Phys. Rep.* **2011**, *498*, 189-241. [DOI](#)
115. Zhu, H.; Fu, Y.; Meng, F.; et al. Lead halide perovskite nanowire lasers with low lasing thresholds and high quality factors. *Nat. Mater.* **2015**, *14*, 636-42. [DOI](#)
116. Fu, Y.; Zhu, H.; Schrader, A. W.; et al. Nanowire lasers of formamidinium lead halide perovskites and their stabilized alloys with improved stability. *Nano. Lett.* **2016**, *16*, 1000-8. [DOI](#)
117. Zhang, Q.; Ha, S. T.; Liu, X.; Sum, T. C.; Xiong, Q. Room-temperature near-infrared high-Q perovskite whispering-gallery planar nanolasers. *Nano. Lett.* **2014**, *14*, 5995-6001. [DOI](#) [PubMed](#)
118. Meng, K.; Gao, S.; Wu, L.; et al. Two-dimensional organic-inorganic hybrid perovskite photonic films. *Nano. Lett.* **2016**, *16*, 4166-73. [DOI](#)
119. Zhang, H.; Zou, C.; Chen, Y.; et al. Continuous-wave vertical cavity surface-emitting lasers based on single crystalline lead halide perovskites. *Adv. Opt. Mater.* **2021**, *9*, 2001982. [DOI](#)
120. Pourdavoud, N.; Wang, S.; Mayer, A.; et al. Photonic nanostructures patterned by thermal nanoimprint directly into organo-metal halide perovskites. *Adv. Mater.* **2017**, *29*, 1605003. [DOI](#)
121. Pourdavoud, N.; Mayer, A.; Buchmüller, M.; et al. Distributed feedback lasers based on MAPbBr<sub>3</sub>. *Adv. Mater. Technol.* **2018**, *3*, 1700253. [DOI](#)
122. Shao, Z.; Wang, Z.; Li, Z.; et al. A scalable methylamine gas healing strategy for high-efficiency inorganic perovskite solar cells. *Angew. Chem. Int. Ed.* **2019**, *58*, 5587-91. [DOI](#)
123. Zhuang, J.; Liu, C.; Kang, B.; et al. Rapid surface reconstruction in air-processed perovskite solar cells by blade coating. *Adv. Mater.* **2024**, *36*, e2309869. [DOI](#)